NAVAL POSTGRADUATE SCHOOL

MONTEREY, CALIFORNIA

DISSERTATION

WAVE EVOLUTION IN RIVER MOUTHS AND TIDAL INLETS

by

Douglas W. Pearman

June 2014

Dissertation Supervisor: Thomas H. C. Herbers

Approved for public release; distribution is unlimited

THIS PAGE INTENTIONALLY LEFT BLANK

REPORT DOCUMENTATION PAGE			*Form Approved OMB No. 0704-0188*
Public reporting burden for this collection of information is estimated to average 1 hour per response, including the time for reviewing instruction, searching existing data sources, gathering and maintaining the data needed, and completing and reviewing the collection of information. Send comments regarding this burden estimate or any other aspect of this collection of information, including suggestions for reducing this burden, to Washington headquarters Services, Directorate for Information Operations and Reports, 1215 Jefferson Davis Highway, Suite 1204, Arlington, VA 22202-4302, and to the Office of Management and Budget, Paperwork Reduction Project (0704-0188) Washington DC 20503.			
1. AGENCY USE ONLY *(Leave blank)*	**2. REPORT DATE** June 2014	**3. REPORT TYPE AND DATES COVERED** Dissertation	
4. TITLE AND SUBTITLE WAVE EVOLUTION IN RIVER MOUTHS AND TIDAL INLETS		**5. FUNDING NUMBERS**	
6. AUTHOR(S) Douglas W. Pearman			
7. PERFORMING ORGANIZATION NAME(S) AND ADDRESS(ES) Naval Postgraduate School Monterey, CA 93943-5000		**8. PERFORMING ORGANIZATION REPORT NUMBER**	
9. SPONSORING /MONITORING AGENCY NAME(S) AND ADDRESS(ES) N/A		**10. SPONSORING/MONITORING AGENCY REPORT NUMBER**	
11. SUPPLEMENTARY NOTES The views expressed in this thesis are those of the author and do not reflect the official policy or position of the Department of Defense or the U.S. Government. IRB Protocol number ____N/A____.			
12a. DISTRIBUTION / AVAILABILITY STATEMENT Approved for public release; distribution is unlimited		**12b. DISTRIBUTION CODE**	

13. ABSTRACT (maximum 200 words)

Detailed observations of wave evolution and wave-current interaction in tidal inlets and river mouths are essentially non-existent owing to the difficulty of installing and maintaining fixed instruments in this harsh environment. This work develops and explores the use of small, free-drifting buoys to collect wave and current measurements in coastal inlets. The instruments, referred to as Wave-Resolving Drifters (or WRDs), are small, lightweight and inexpensive enough to be deployed and retrieved in large numbers from small vessels. To study wave evolution in the San Francisco Bight and the Mouth of the Columbia River, 30 WRDs are deployed during peak ebb tide so that the drifters flow into the incident wave field. Wave statistics estimated through local ensemble averaging of drifter observations and ensemble-averaged wave spectra are used to describe the wave evolution through the inlet area. The observations reveal dramatic spatial variability in the wave field and sometimes doubling of the local wave heights. Comparisons with numerical simulations of the SWAN (Simulating Waves Near Shore) model and geometric optics theory (ray diagrams) show the distinct effects of refraction by variable shoals and currents on the wave field and hint at nonlinear instabilities that may cause rogue wave development.

14. SUBJECT TERMS Wave-current interaction; river mouth; tidal inlet; drifter observation; Lagrangian sensing; refraction; ray theory; extreme waves; rogue waves.			**15. NUMBER OF PAGES** 105
			16. PRICE CODE
17. SECURITY CLASSIFICATION OF REPORT Unclassified	**18. SECURITY CLASSIFICATION OF THIS PAGE** Unclassified	**19. SECURITY CLASSIFICATION OF ABSTRACT** Unclassified	**20. LIMITATION OF ABSTRACT** UU

NSN 7540-01-280-5500

Standard Form 298 (Rev. 2-89)
Prescribed by ANSI Std. 239-18

THIS PAGE INTENTIONALLY LEFT BLANK

WAVE EVOLUTION IN RIVER MOUTHS AND TIDAL INLETS

Douglas W. Pearman
Lieutenant Commander, United States Navy
B.A., Thomas Edison State College, 2006
M.S., University of Southern Mississippi, 2007
M.S., Naval Postgraduate School, 2011

Submitted in partial fulfillment of the
requirements for the degree of

DOCTOR OF PHILOSOPHY IN PHYSICAL OCEANOGRAPHY

from the

NAVAL POSTGRADUATE SCHOOL
June 2014

Author:

_____
Douglas W. Pearman

Approved by:

_____   _____
Thomas H. C. Herbers   Jamie H. MacMahan
Professor of Oceanography   Associate Professor of
Dissertation Supervisor   Oceanography

_____   _____
Mary Batteen   Patrick Harr
Professor of Oceanography   Professor of Meteorology

_____   _____
Tim T. Janssen   Todd Holland
Research Scientist   Supervisory Oceanographer

Approved by: _____
Peter Chu, Chair, Department of Oceanography

Approved by: _____
Douglas Moses, Vice Provost for Academic Affairs

iii

THIS PAGE INTENTIONALLY LEFT BLANK

ABSTRACT

Detailed observations of wave evolution and wave-current interaction in tidal inlets and river mouths are essentially non-existent owing to the difficulty of installing and maintaining fixed instruments in this harsh environment. This work develops and explores the use of small, free-drifting buoys to collect wave and current measurements in coastal inlets. The instruments, referred to as Wave-Resolving Drifters (or WRDs), are small, lightweight and inexpensive enough to be deployed and retrieved in large numbers from small vessels. To study wave evolution in the San Francisco Bight and the Mouth of the Columbia River, 30 WRDs are deployed during peak ebb tide so that the drifters flow into the incident wave field. Wave statistics estimated through local ensemble averaging of drifter observations and ensemble-averaged wave spectra are used to describe the wave evolution through the inlet area. The observations reveal dramatic spatial variability in the wave field and sometimes doubling of the local wave heights. Comparisons with numerical simulations of the SWAN (Simulating Waves Near Shore) model and geometric optics theory (ray diagrams) show the distinct effects of refraction by variable shoals and currents on the wave field and hint at nonlinear instabilities that may cause rogue wave development.

THIS PAGE INTENTIONALLY LEFT BLANK

TABLE OF CONTENTS

LIST OF FIGURES

THIS PAGE INTENTIONALLY LEFT BLANK

LIST OF TABLES

THIS PAGE INTENTIONALLY LEFT BLANK

LIST OF ACRONYMS AND ABBREVIATIONS

Cos   cosine

DWR-G   Datawell Wave Rider-GPS

FFT   Fast Fourier Transform

GPS   Global Positioning System

H_s Significant Wave Height

Hz   hertz

IMU   Inertial measurement unit

JONSWAP   Joint North Sea Wave Program

km   kilometer

MCR   Mouth of the Columbia River

MEMS   Micro-Electro Mechanical Systems

ms^{-1} meters per second

NOAA   National Oceanic and Atmospheric Administration

RADAR   RAdio Detecting and Ranging

R/V   research vessel

SELFE   Semi-Explicit Lagrangian Finite Element

SF Bar   San Francisco Bar

Sim   simulation

Sin   sine

SWAN   Simulation of Waves Nearshore

USACE   United States Army Corps of Engineers

USGS   United States Geological Service

WNW   West-Northwest

WRD   Wave Resolving Drifter

THIS PAGE INTENTIONALLY LEFT BLANK

ACKNOWLEDGMENTS

I would like to express my sincere gratitude to Prof. Tom Herbers, whose knowledge and guidance were instrumental in ensuring the success of the research that makes up this dissertation. His excitement for the science was matched only by his willingness to attempt innovative methods in ocean sensing.

I am grateful for the opportunity to have had Dr. Tim Janssen as a mentor through this program, fieldwork partner, co-author and friend. His timely advice and patience with my aggressive deadlines were greatly appreciated.

To Professor Jamie MacMahan, whose train of thought I disrupted on a somewhat regular basis, thanks for the many discussions (and for inviting me join the Littoral Field Studies class a second time)!!!

Professor Mary Batteen, thanks for periodically checking on my progress to make sure I was on track.

I would like to thank Professor Pat Harr, who was also my master's thesis advisor, for agreeing to participate in this effort in spite of having just completed a thesis with me.

To Dr. Todd Holland from NRL SSC, I can't express my gratitude enough. We have worked on various projects together since I was a Chief. I truly appreciate the patience, guidance, multiple letters of recommendation, mentorship and general friendship he has extended to me over the years.

Thanks to all of my friends, but special thanks to Steve McIntyre and Jeff Portell for putting the extra effort into your thesis work in order to support this research!

Most importantly, to my beautiful bride of 20 years, Holly, no words can express how much I appreciate you. You have been patiently supportive of every crazy adventure on which I have embarked. So, thank you once again. I would not be where I am today without you. To my girls, Cienna and Hannah, I appreciate your patience through all of the missed events and for pretending to be interested in our discussions about the science!

THIS PAGE INTENTIONALLY LEFT BLANK

I.   INTRODUCTION

Tidal inlets and river mouths are the shipping gateways between the oceans and rivers for commercial vessels and the U.S. Navy. Along the west coast of the United States two of these major gateways are the Golden Gate in the San Francisco Bight and the Mouth of the Columbia River where the interaction of tidal currents, complicated shoal systems and ocean waves can make for hazardous navigation conditions.

The strait under the Golden Gate Bridge connects the San Francisco Bay and its complex estuary system, which is the largest estuary on the Pacific Coast, to the Pacific Ocean. The combined economic impact of the Port of San Francisco and the Port of Oakland is estimated to be about 4 billion dollars each year (San Francisco Port Authority). To reach these two ports, more than 4,000 ships that pass through the Golden Gate each year must transit along a shipping channel that splits the bifurcated shoal system of the Four Fathom Bank and the South Shoal. This region, known as the San Francisco Bight, is open to the predominantly west-northwest swell conditions that can pose a significant hazard to navigation when they steepen in response to the shoal system. San Francisco Bay is also known to have very strong ebb tidal currents (about $2 \mathrm{~m~s}^{-1}$) that interact with and further complicate the wave field. The safest navigation path is to stay in the channel, but that too can be dangerous in some wave conditions (San Francisco Port Authority).

An estimated 3600 ocean-going vessels pass through the Mouth of the Columbia River making their way to Portland, OR (Columbia River Bar Pilots). These vessels must pass over the treacherous region known as the graveyard of the Pacific, or the Bar, as the local mariners know it. When westerly approaching ocean waves interact with the complicated shoal system outside the mouth of the Columbia River dangerous wave conditions can occur. The natural drainage of the Columbia River couples with a large semi-diurnal tide resulting in a strong ebb tidal jet with velocities that can exceed $4 \mathrm{~m~s}^{-1}$ as it exits the shoal system. This strong current enhances the already rough wave conditions over the bar, and extreme wave conditions, or rogue waves, can result (Oregon State Marine Board).

This dissertation investigates evolution of the waves in the approaches to the San Francisco Bay and the Mouth of the Columbia River. Traditional measurement approaches that require moored instrumentation are helpful, but the highly variable nature of a wave field interacting with a complicated shoal system, and the inherent difficulty of maintaining fixed instruments in a shipping channel with strong currents make that approach impractical. Therefore, a fleet of 50 wave-resolving drifters (WRD) that measure positions and horizontal velocities with GPS data-loggers and vertical accelerations with accelerometers was developed. The use of these instruments was explored with multiple deployments at both field sites, but this work a focuses on a single deployment from each site that best highlights the new application of this technology and identifies the physical mechanisms that influence the wave fields. Chapter II outlines the drifter development, deployment and analysis technique as well as the analysis of wave evolution in the San Francisco Bight. In Chapter III, a similar analysis is applied to the Mouth of the Columbia River where extreme waves were observed. Finally, Chapter IV summarizes the findings and discusses possible future work.

II. DRIFTER OBSERVATIONS OF WAVE EVOLUTION IN SAN FRANCISCO BIGHT

A. INTRODUCTION

In coastal areas characterized by strong currents and energetic waves, such as in and near tidal inlets, *in situ* measurements of waves and currents are very difficult to make. In particular, the use of standard measurement techniques, using bottom-mounted or moored instruments, is complicated due to e.g. the distortion of buoy response by current drag on mooring lines (Anctil et al. 1993; Steele 1997; de Vries et al. 2003), burying of instruments by dynamic seabed morphology (e.g., Barnard et al. 2006), and loss or damage of instruments by ship traffic (Elias et al. 2012). Moreover, waves and currents generally undergo strong spatial variations in coastal inlets and this spatial evolution and inhomogeneity is difficult to capture with a limited number of fixed instruments. As a consequence, synoptic observations of wave-current interaction and wave evolution in such regions are extremely rare, which hampers progress in understanding these dynamics in natural inlets.

In the present work, we explore the use of instrumented drifters to resolve wave-current interactions in the approaches to and inside of a coastal inlet. Such free-drifting instruments can be readily deployed in these environments and, when used in large numbers, can provide synoptic information on the variability of waves and currents in the area of interest. The observations are Lagrangian (not Eulerian), and in regions with strong currents and spatially variable wave fields, recorded time series can be highly non-stationary (even if the wave conditions are fairly stationary from an Eulerian point of view). However, by deploying a large number of drifters, reliable statistical estimates can be obtained through ensemble averaging of statistical quantities estimated from short time series of nearby drifter measurements.

In the past, GPS drifters have been used extensively to measure ocean currents and surf zone dispersion (MacMahan et al. 2009), but recent advances in GPS technology have made it possible to simultaneously collect both wave and current measurements, even with inexpensive GPS receivers (Herbers et al. 2012). Although the absolute

position accuracy for inexpensive off-the-shelf GPS receivers is somewhere between 2.5 m and 10 m, these errors fluctuate on time scales much longer than the periods of wind waves and swell and thus do not significantly affect wave measurements (Herbers et al. 2012). Moreover, Doppler velocity measurements, which are also available on most GPS receivers, are far less sensitive to so called "jumps" when satellites enter and leave the useable horizon. As a consequence, using the Doppler velocities rather than positions, generally results in cleaner signal and better resolution over short time intervals, which can be particularly important in the wind wave band (Thomson 2012).

The drifters developed in this study utilize the Doppler velocity measurements from the same GPS receivers (Locosys GT-31) as those used by Herbers et al. (2012), but the sensor package is augmented with an accelerometer to resolve vertical motions and higher-frequency waves. By resolving both the horizontal and vertical wave orbital motions, we remove a 180-degree ambiguity in directional estimates based on horizontal GPS measurements alone (see Herbers et al. 2012). The procedure enables the accurate measurement of strongly nonlinear waves (e.g., near breaking and steep waves on opposing currents).

The objective of the present work is twofold. The first objective is to validate the improved drifter sensor package in a natural (random) wind wave field. In particular we test the ability of the new motion sensor package that combines the GPS and accelerometer measurements to resolve vertical motions at higher frequencies than was possible with the drifters used in Herbers et al. (2012). This is an important improvement, which will greatly enhance the potential of these drifting buoys for wave observations. We test this new capability by deploying drifters alongside a Datawell Waverider buoy in relatively homogenous open ocean conditions, and compare the frequency and directional spectra of the different buoys.

The second objective is to use the wave-resolving drifters (WRDs) to study wave evolution in a natural inlet, thus exploring their use in regions characterized by strong currents. A goal is to develop a reliable analysis technique that can be used to investigate the physical processes that drive wave evolution in a tidal inlet. To this end, we deployed large numbers of WRD during ebb currents in the San Francisco Bight (Figure 1) to

observe the interactions of wind waves and swell with strong opposing currents. The nonstationary nature of the data records, caused by the rapid transit of the drifters through the channel and over the ebb tidal shoal, complicates the analysis. Here, we show that robust estimates of wave spectra and bulk statistics can be obtained from these records by ensemble averaging short-time estimates over many drifters. Additionally, ray diagrams and simulations from a SWAN wave model, one-way coupled with a Delft3D FLOW model, are used to identify the physical mechanisms responsible for the changes in the wave field in the approaches to and in the tidal inlet as seen in the drifter observations.

The San Francisco Bight field experimental site and drifter sensor package design are described in section B. The wave-current model implementation is outlined in section C, and the observed wave evolution is compared to model predictions in section D. Finally, we summarize our findings in section E.

B.   FIELD SITE AND INSTRUMENTATION

1.   Field Site

The San Francisco Bay is a large tidal estuary that is connected to the Pacific Ocean by a narrow inlet. The bay side (east) of the inlet is spanned by the Golden Gate Bridge at the narrowest point, and the west side of the inlet opens to the Pacific Ocean. A mixed semi-diurnal tidal cycle that consists of a 28-day spring and neap cycle (NOAA, 2009) results in strong tidal forcing through the inlet where the currents can exceed 2.5 m s^{-1} near the inlet mouth and maintain velocities of 1 m s^{-1} to the ebb tidal shoal approximately 8 km offshore (Barnard et al. 2006; Elias et al. 2012; and Barnard et al. 2012).   Waves approaching the San Francisco Bight from a predominantly west-northwest direction interact with a complex shoal area bathymetry and a strong ebb tidal jet (Elias and Hansen 2012 and references therein).

2.   Wave Resolving Drifters

The drifters developed and used in this study were designed as lightweight instrument packages that can be deployed from small vessels and accurately resolve both ocean surface waves and currents. The drifter itself consists of a 30 cm diameter, hard

shell, closed-cell foam core buoy (Jim-Buoy model 4400-RF) with a 1.25 cm wide rubber band attached near the waterline to mitigate the immersion buoyancy resonance that occurs at 1.11 Hz for this drifter. A ballast weight (10.4 kg) is suspended from a shackle to submerge the buoy approximately to the centerline (see Figure 1).

The wave-current sensor package attached to the buoy consists of a GPS receiver (Locosys GT-31), and a three-axis accelerometer package (Gulf Coast Data Concepts X6-2). The latter is tethered between the buoy and the ballast chain (Figure 1) to maintain a nearly vertical orientation of the accelerometer, irrespective of the buoy orientation. This design suppresses the sensitivity to roll and pitch motions of the buoy vertical acceleration measurements that can result from steeper, high-frequency waves.

To allow real-time tracking of the drifter's position, which is essential as a recovery aid when deploying large numbers of drifters close to shore in strong currents, the drifter is equipped with a Garmin DC 40 GPS transmitter.

a.   GPS Position and Velocity Sensor

The Locosys GT-31 GPS receiver, based on the SiRF III chipset, collects data at 1Hz and accurately resolves the horizontal components of the wave orbital displacements using differential position data (see Herbers et al. 2012). Additionally, estimates of horizontal velocity can be extracted from the Doppler shifts in the raw L1 carrier phase signals. The resolution of the Doppler velocity data is an order of magnitude higher than the differential positioning data, which particularly improves the accuracy of high-frequency wind-wave measurements (Thomson 2012). In these experiments both horizontal Doppler velocity and differential positions were recorded and analyzed.

Herbers et al (2012) show that the GT-31 sensors yield accurate and reliable wave energy and direction spectra. However, vertical motions cannot be accurately resolved with these inexpensive GPS receivers. Although the horizontal motions alone can be used to estimate wave statistics (as shown by Herbers et al. 2012), this requires the use of linear wave theory, which is less reliable in very steep waves, and wave direction estimates based on horizontal motions alone suffer from a 180-degree ambiguity (Herbers et al. 2012).

b.   *Accelerometer*

To augment the GPS sensor and resolve the vertical motions, a three-axis accelerometer (X6-2 MEMS) manufactured by Gulf Coast Data Concepts, LLC was added to the sensor package. The accelerometer measures vertical accelerations in the range of +/- 2 g, where g is the gravitational acceleration $\left(9.81\ \text{m s}^{-2}\right)$. The sampling rate is 10 Hz, and acceleration fluctuations as small as $0.001\ \text{m s}^{-2}$ are resolved, which make this accelerometer well suited to the measurement of surface-wave accelerations that are typically a small fraction of gravity (g). Since the X6-2 is a stand-alone accelerometer and not part of an inertial measurement unit (IMU), it does not resolve the body orientation so that the vertical accelerations may contain errors due to changes of the pitch and roll of the sensor during the motion. However, these errors are likely small as the sensor was tethered between the buoy and the ballast chain, thus suppressing the pitch and roll motions induced by the sea surface slope.

The accelerometer wave measurements are noisy at low swell frequencies where the signal-to-noise ratio suffers from small accelerations (low steepness of these longer waves) and contamination by nonlinear buoy motions (Appendix A).

c.   *Integrated Sensor Package*

To account for the different sample rates, the accelerometer and GPS time series were interpolated onto a common 10 Hz time base (see McIntyre 2013 for more details). The accelerometer is capable of resolving high-frequency motions, but its accuracy is degraded at lower frequencies (< 0.15 Hz). On the other hand, the GPS receiver is most accurate in the swell frequency band (~0.05 – 0.15 Hz) but becomes increasingly noisy at higher frequencies (Herbers et al. 2012). Therefore, to obtain an accurate measurement of the wave statistics and the wave spectrum across the complete frequency range, covering both the swell and wind wave bands, we estimate a composite spectrum that combines the GPS (lower-frequency range) and accelerometer (higher-frequency range). Specifically, we use the GPS observations in the range 0.05 Hz – 0.15 Hz and vertical accelerations (from accelerometer) in the range 0.25 Hz – 1 Hz. In the intermediate range

7

(0.15 Hz – 0.25 Hz) the spectrum is determined from a weighted average of the two sensors, where the GPS (accelerometer) weighting was varied linearly from 1(0) at 0.15 Hz to 0(1) at 0.25 Hz. The swell peak is well resolved in the combined sensor spectrum (Figure 2), in good agreement with the Datawell estimate, and the high-frequency tail closely follows the f^{-4} (Phillips 1984) high-frequency slope out to the 1.11 Hz maximum frequency that can be resolved by the Wave Resolving Drifter (WRD) buoy. In Figure 2 the Datawell spectrum is shown only out to 0.32 Hz because of its lower sampling rate (1.28 Hz) and immersion resonance frequency (0.7 Hz). Additionally, H_s estimates from the WRD are within 3% of the Datawell buoy estimates, which was used for ground truth in the validation. A detailed discussion of the methodology and validation is provided in Appendices A and B.

C.   WAVE-CURRENT MODEL IMPLEMENTATION

To support the analysis of the observations collected in the San Francisco Bight, a region characterized by complicated bathymetry and strong currents, we implemented the third-generation wave model SWAN, one-way coupled to the Delft3D circulation model for this area (see Elias and Hansen, 2012). The wave model SWAN is based on the action balance equation (Booij et al. 1999 and Ris et al. 1999), which can be expressed as

$$\frac{\partial N}{\partial t} + \Delta_{x,y} \cdot \left[\left(\vec{c}_g + \vec{U} \right) N \right] + \frac{\partial}{\partial \theta} \left(c_\theta N \right) + \frac{\partial}{\partial \sigma} \left(c_\sigma N \right) = \frac{S_{tot}}{\sigma} \; , \tag{1}$$

where the source terms can be written as

$$S_{tot} = S_{in} + S_{wc} + S_{nl4} + S_{bf} + S_{brk} \; . \tag{2}$$

The left side of equation (1) represents the conservation of the action density $N(\sigma, \theta; x, y, t) = \frac{E}{\sigma}$, where E is energy, σ is relative frequency (moving reference frame), θ is wave direction, and $x, y,$ and t represent the horizontal coordinates and time, respectively. The current field is represented by $\vec{U}$, $\vec{c}_g$ is the (linear) group speed, and c_θ and c_σ represent transport rates in directional and frequency space, respectively (see Booij et al., 1999).

The source term (the right side of equation (1)) settings are as follows. The wind input, S_{in}, was set to the default 3rd generation Cavaleri and Malanotte-Rizzoli (1981) parameterization, the whitecapping term S_{wc} was set to Van der Westhuysen et al. (2007), nonlinear quadruplet interactions, S_{nl}, were computed with the standard Discrete Interaction Approximation (Hasselmann et al, 1985), bottom friction S_{bf} was set to Hasselmann et al. (1973) using the swell setting, and the Battjes and Janssen (1978) formulation was used for depth-induced wave breaking S_{brk}.

The SWAN simulations were done in nonstationary mode and finite differences were solved on an unstructured grid with minimum resolution offshore and maximum resolution in the region of interest. To accurately resolve refraction effects of the swell band over the complicated medium variations in this area, we applied a 2-degree resolution for the wave directional space in our model implementation. The offshore boundary conditions were obtained from the spectral estimates from wave measurements made by the Point Reyes NOAA buoy #46214 (Figure 3).

The wind forcing was separated into two regions. The wind measurement time series from the NOAA San Francisco Buoy #46026 (located 33 km offshore) was applied uniformly in the domain seaward of the mouth of the inlet, and the time series from the NOAA station #FTPC1 located just inside the inlet on the south of the channel was used for the inlet (small box in Figure 3). The wind measurements from these locations were found to be reasonably representative (within 3 m s^{-1} on average) of the measurements made by the shipboard anemometer while transiting these regions at coincident times.

The currents $(\vec{U})$ were simulated using the Delft3D flow model using the implementation for the San Francisco Bay developed by Elias and Hansen (2012), which was developed to investigate sediment transport in regions around the San Francisco Bay and Bight (see Elias and Hansen 2012; Barnard et al. 2012). The circulation model consists of six decomposed (2-way coupled) domains that allow for varying resolution, and results in a spatial resolution of about 50 m in our region of interest (the San

Francisco Bight). Due to the extensive scale of the full domain, this model was run in depth-averaged mode to gain computational efficiency (Elias and Hansen 2012).

The SWAN model domain used in this study extends 50 km north and south of the Golden Gate and 50 km offshore to the Point Reyes buoy (see Figure 3). A comparison of the spectra and significant wave height (H_s as defined in Appendix A) observed at the San Francisco NOAA Buoy just outside our region of interest shows reasonably good agreement with the SWAN simulation (Figure 4). A synoptic view of the current field and predicted significant wave heights at peak ebb flow (Figure 5) shows the expected strong variability of waves with amplification over the bar and in the current jet.

To isolate the effects of different physical mechanisms and forcing on the observed wave evolution, various SWAN simulations were conducted with alternately wind forcing, current or bottom friction turned off.

D.   RESULTS

1.   Drifter Observations

To study wave evolution in the San Francisco Bight during an ebb tide, we deployed an array of 30 WRDs near the Golden Gate on April 27, 2012 (see Figure 1). The WRDs were placed near the center of the ebb tidal jet, so that (with few exceptions) they were carried across the ebb tidal shoal (labeled SF Bar in Figures 1 and 3) through the opposing wave field. The large array of drifters allowed for ensemble averaging to estimate wave spectra and bulk statistics from the non-stationary time series collected by the drifters as they traversed the spatially inhomogeneous wave field across the inlet.

To capture the ebb tidal cycle, the deployments started about 1.5 hours before predicted peak ebb current (1.88 m s^{-1}), near the seaward entrance to the San Francisco Bay inlet. They were deployed in clusters of five under the Golden Gate Bridge with one minute spacing between each drifter in a cluster and six minutes between each cluster. The last WRD was deployed near the time of peak ebb current, which ensured that all the WRD would depart the mouth of the inlet as the ebb tide began to slacken.

Since the drifters were carried by the fast flowing ebb current (surface flows approaching 2 m s^{-1}) through a spatially inhomogeneous wave field, the time series recorded by the individual drifters are non-stationary. To enable the use of standard time series analysis techniques (assuming stationarity), we divide the observations in relatively short segments (4096 samples at 10 Hz or roughly 6.8 minutes), and to improve statistical reliability, we average spectral estimates over ensembles of drifters that pass through the same area.

The nearly uniform lateral expansion of the drifters as they exit the channel (see Figure 6a), allows us to estimate wave statistics through spatial averaging onto a regular 500 m x 500 m grid and thus obtain a synoptic view of the wave variability in the area of interest. Figure 6a shows the ensemble-averaged H_s for each grid cell plotted on the data centroid of the drifter ensemble locations. The number of drifter observations per grid cell varies across the spatial domain, and the resulting ensemble sizes vary from a single drifter estimate at certain points on the outer edges of the drift tracks, to up to 40 in the well-traveled areas in the middle of the jet.

Over the San Francisco Bar (SF Bar), a dramatic increase in wave height (locally up to 3 m) is followed by a fairly abrupt decrease to about 1.6 m immediately east of the SF Bar. Approaching the inlet, the wave heights again increase as the waves encounter the strong tidal jet, followed by a dramatic decrease inside the inlet. A similar wave height pattern, albeit with smaller with more gradual variations, is defined by the SWAN simulation (Figure 6b).

Additionally, ensemble-average spectra were computed in five regions where the wave characteristics in the WRD observations are similar. The regions (see Figure 6a) were defined as follows: Region A (offshore, ensemble average of 489 spectra), Region B (SF Bar, 273 spectra), Region C (east of the SF Bar, 157 spectra), Region D (approach to the inlet entrance, 270 spectra), and Region E (inside inlet, 172 spectra).

In the discussion that follows, we will focus the analysis on spectral bands, defined here as the swell band (0.05 Hz – 0.15 Hz), the wind sea band (0.15 Hz – 0.3 Hz), and the spectral tail (0.3 Hz – 1.0 Hz). We will compare observed variability of

these bands to SWAN simulations, while varying the various forcing terms in the model simulations (to isolate the effect of each forcing term), combined with ray computations, to identify the dominant physical mechanisms that cause the observed variability in this region.

The discussion in each section will progress from offshore into the inlet, thus following the wave field (as opposed to the drifters) as it evolves through the inlet.

2. Swell Band

The WRD estimates of H_s (dominated by ~11 s swell) increase progressing from offshore to over the SF Bar (Figure 6a), and a similar increase is apparent in the default SWAN Sim #1 (Figure 6b). There is a sharp amplification in the swell band of the observed and predicted spectral estimates (Figure 7a, b), indicating that the wave height variability in this region is predominantly related to swell focusing on the bar. The effects of shoaling due to the decrease in group speed c_g only account for about 10% of the amplification in wave height. The main cause for the wave height increase is the strong refractive focusing that is evident in the ray trajectories (Figure 8). A comparison of the rays computed with currents (Figure 8a) and without currents (Figure 8b) shows little change and suggests that the focusing is predominantly in response to the refractive effect of variable water depth over the bar. In SWAN Sim#4 (Figure 9c) only marginally less amplification occurs over the bar, which also suggests that the amplification is due to bottom refraction.

Continuing east across the bar, the observed abrupt decrease in H_s (see Figure 6a) is also evident in all SWAN simulations. However, this decrease is most pronounced in Sim #2 where the disabling of wind forcing accentuates the swell wave variability. The abrupt decrease of nearly 1m in wave height (Figure 6a) and the similar drop in swell spectral levels seen in both the WRD and SWAN results (Figures 7a and 7b) cannot be explained by bottom friction alone as the waves transit the bar, which is confirmed by Sim #3 (Figure 9b) where bottom friction is disabled yet a similar reduction in wave height occurs. The orientation of the north bar and the SF Bar relative to the prevailing swell arriving from the WNW results in strong refractive effects. The dramatic decrease

12

of energy in the swell band in this region is associated with the divergence of the ray trajectories in the lee of the bar (Figure 8a). These strong refraction effects are also evident in the directional spread estimates from the WRD (Figure 10) that increase from less than 20 degrees seaward of the bar to greater than 30 degrees behind the bar. A comparison of the rays with currents (Figure 8a) and without currents (Figure 8b) as well as SWAN Sim #1 (Figure 6b with currents) and Sim #4 (Figure 9c without currents), shows that the effects of the current field on the swell is negligible. This shows that the large difference in wave height observed between the bar and to the region just to the east of it, is principally due to refractive focusing by the bathymetry.

Progressing east, a slight amplification is observed in Region D (Figure 6a), which - to a lesser degree – is also evident in the SWAN simulations (e.g. Sim #2 without wind, Figure 9a). However, the limited increase of spectral energy levels in the swell band (Figure 7a) does not account for the overall increase in H_s as evident in Figure 6a, which suggests that changes in the other frequency bands are important here as well (which is discussed in the following).

When progressing farther into the channel, the observed and predicted H_s again decrease abruptly (Figure 6a). The decay is especially strong in the swell band (Figure 7a, b) and appears to be caused by refraction due to varying depth (note the ray divergence over the deeper channel in Figure 8a, b), although diffractive effects of the channel (Melo and Guza 1991), which are not accounted for in SWAN, may also be important. Although the refraction on the jet-like ebb current will likely oppose somewhat the refractive divergence induced by the bathymetry in this region, the (longer) swell waves are more sensitive to variations in the bathymetry than the current field.

3.   Wind-wave Band

In this section we focus on the evolution of less energetic, higher-frequency waves using the average spectra in regions A-E. Offshore of the SF Bar, the wind wave band (Figure 7a) is characterized by a slight elevation in energy near 0.2 Hz that extends to 0.3 Hz before it rolls off into the f^{-4} spectral tail (similar to the spectrum from homogenous open ocean conditions in Figure 2). The currents in the offshore region are

less than 0.5 $\mathrm{m\,s^{-1}}$, but increase to 1.4 $\mathrm{m\,s^{-1}}$ over the SF Bar. A noticeable increase in energy in the wind wave band is apparent in the spectra (Figure 8a) which results in an increase in the non-dimensional mean steepness parameter, $\varepsilon = \dfrac{H_s k_p}{2}$, (Banner 2000) from 0.04 offshore to 0.07 over the bar (where H_s in the frequency range from 0.15 Hz to 1.00 Hz is considered and k_p is the peak wave number that follows from the linear dispersion relation at the relative frequency peak). The minimum depth on the shoal is 8 m and the ray trajectories indicate that the depth variability does not much affect the propagation of the (relatively short) dominant wind waves. However, current refraction (Figure 10a) causes a slight convergence on the northeast portion of the SF Bar.

Contrary to what was observed in the swell-band (where a strong decrease was seen), the region east of the bar exhibits a marked increase in energy, in the wind-wave band (Figure 7a). The surface velocity in this region increases to a mean of 1.88 $\mathrm{m\,s^{-1}}$ resulting in further steepening (mean steepness parameter of $\varepsilon = .11$) as the waves steepen on the current (Bascheck et al. 2006) and ray trajectories including the currents (Figure 11a) show pronounced focusing in this region of amplified wind wave energy. Rays without currents (Figure 11b) show virtually no focusing in this region (or anywhere else for that matter). These results indicate that the waves in this band are refracting onto the strengthening ebb tidal jet, which explains the increase in energy, and steepening ($\varepsilon = 0.11$) observed in this region.

Approaching the entrance to the inlet, the energy levels in the wind-wave band continue to increase (Figure 7a), and despite the marked decrease in swell energy there is an increase in overall H_s in this region, as wave conditions change from swell-dominated to wind-wave dominated. The ebb tidal jet is very focused in this region (see Figure 5) and the surface currents reach a maximum mean velocity (1.89 $\mathrm{m\,s^{-1}}$). Additionally the north shoal (where the shallowest depths are around 4 m) refracts the wind sea waves into the channel, where they are superposed by waves directly incident onto the inlet mouth and enhanced by the current jet (compare Figure 11a and 11b). The mean steepness parameter in this region reaches 0.15, which indicates a high probability

of breaking (Banner 2000). Current-induced refraction on the ebb tidal jet and steepening on the opposing current, results in a region of enhanced directional spreading and steepness in this band.

Finally, entering further into the inlet, spectral energy levels drop dramatically, in part attributed to refraction as ray trajectories for both swell and wind-wave frequencies show a strong divergence in the channel (Figures 8a, 11a). Breaking dissipation of high-frequency waves, steepening on the opposing current, may also contribute to the observed decay. Additionally, the surrounding terrain provides considerable sheltering in this region, resulting in a dramatic decrease in wind forcing conditions within the inlet itself (ship observations were below 4 $\mathrm{m\,s^{-1}}$ in the inlet), virtually eliminating any regeneration of the wind waves on the strong current.

4.   High-frequency Tail

Moving from offshore to the SF Bar (region B in Figure 8), the high-frequency tail shows a slight decrease in the slope at frequencies above the local (linear) blocking frequency (0.54 Hz, estimated from $f_{r,br} = \dfrac{g}{4\pi U}$). This decrease is not observed in the SWAN simulations where the parameterized f^{-4} slope persists.

Progressing inside the bar (Region C), the slope of the high-frequency tail begins to deviate from f^{-4} at lower frequencies presumably in response to the decreased blocking frequency (0.42 Hz) associated with the stronger current in this region. Decrease in high-frequency energy levels in this region is indicative of wave breaking dissipation. This is consistent with an enhanced mean steepness parameter, $\varepsilon = 0.11$, which is significantly larger than the critical value $\varepsilon = 0.05$ suggested by Banner (2000).

Approaching the mouth of the inlet (region D in Figure 8), a further decrease is observed in slope of the high-frequency tail further decreases that is absent in the SWAN results, which suggests enhanced dissipation of high-frequency waves is occurring as they steepen in response to the current.

15

Finally, within the inlet (region E), the decrease in the high-frequency spectral levels, visible in both the WRD and SWAN spectral estimates (Figures 7a and 7b) may be caused by blocking and dissipation on the opposing current, preventing these short waves to enter this region. This combined with much-reduced wind velocities due to sheltering effects, eliminates the re-generation of high-frequency waves in this region.

E. SUMMARY AND CONCLUSIONS

Strong tidal currents, energetic waves, and dynamic seabed morphology can make it very difficult to collect observations of waves and currents in coastal inlets using conventional, bottom-mounted instruments. As a consequence, such observations are exceedingly rare. Moreover, it is difficult to capture the regional variability and inhomogeneity typically seen in coastal inlets using an array of fixed instruments. In this work we explore the use of free-floating Lagrangian drifters as an alternative *in situ* sensing strategy for measuring waves and surface currents in tidal inlets. By treating the drifter observations as independent realizations and ensemble average across them to obtain accurate statistical estimates, we are able to study spectral evolution across the inlet and identify the various physical mechanisms that most influence the spatial variability of the wave field across various frequency ranges (swell, wind sea, high-frequency tail).

The wave-resolving drifters (WRD) combine a GPS receiver that records horizontal displacements and Doppler velocities, with a three-axis accelerometer to resolve the vertical motions. The accelerometer extends the WRDs ability to resolve the high-frequency tail of the wind wave spectrum, and removes the 180-degree ambiguity of GPS wave direction estimates (see Herbers et al. 2012). Comparison to a conventional Datawell DWR-G Waverider buoy shows good agreement, with slightly elevated energy levels away from the peak resulting in a positive bias of approximately 3% in significant wave height estimates (Appendix A and B). The mean directions agree to within 1 degree, but the WRD directional spread is approximately 10 degrees greater than the Datawell estimates (Figure 2). This validation confirms that the WRD developed in this study can provide reliable routine heave-pitch-roll type wave measurements and perform at a similar level as the more expensive and larger 3-D GPS drifters evaluated by Herbers et al. (2012).

The drifters developed here are relatively low cost (< $1000). Hence, they can be used in large numbers, which allows for improved estimates of wave spectra and bulk wave statistics through regional ensemble averaging and dense spatial coverage of both wave and current observations.

To explore the use of large drifter arrays to study inhomogeneous wave conditions in coastal inlets, 30 WRD were deployed in the San Francisco Bight. The time series recorded by free-floating drifters in this region with inhomogeneous wave fields and strong currents are generally nonstationary. The analysis used here is based on short time series to ensure statistical stationarity so that standard frequency and directional spectral analysis techniques can be used, and the degrees of freedom of statistical estimates are increased through ensemble averaging of drifter observations onto a spatial grid. The resulting gridded statistics provide a synoptic view of the spatial variability in the wave field and identify regions of similar H_s in which the individual spectra estimated from relatively short segments of the time series were ensemble averaged to produce more statistically robust regional ensemble spectra. These spectra were used in conjunction with SWAN simulations using various combinations of physical processes and ray computations (both with and without currents) to identify the dominant physical mechanisms that result in the spatial variability of the wave conditions in the tidal inlet during strong ebb tidal flow.

The spatial variability of the wave field in the San Francisco Bight observed on the April 27, 2012 peak ebb tide was evaluated in the swell band, wind-sea band and the high-frequency tail. The variability in the swell band was shown to result primarily from shoaling and refractive effects as the waves propagate over the San Francisco Bar from the deep water of the Pacific Ocean. East of the bar, the combined refractive effects of the shoals on either side of the shipping channel results in a divergent swell pattern and a dramatic reduction in swell wave energy. Progressing farther east toward the inlet, the dominant physical mechanism influencing the wave field was the ebb tidal jet causing an increase in energy in the wind-wave band as these short waves steepened (mean steepness parameter increase from 0.04 to 0.15) and refracted onto the ebb tidal jet (maximum current approaching 2 m s^{-1}). In the inlet, there is a drastic decrease in energy

across the spectrum that can be attributed to several factors, including depth induced refractive effects, the blocking and dissipation of short waves (frequencies exceeding 0.42 Hz) due to the strong opposing currents, and a loss of wind forcing owing to sheltering effects of the orography bordering the narrow inlet.

These results show that the drifter ensemble data resolve the two-dimensional wave field evolution across complex bathymetry (San Francisco Bar) and through an ebb tidal jet, providing a unique and synoptic analysis of the various processes affecting wave dynamics in this complicated region, and illustrating the utility of this approach to the study of coastal inlets.

III. WAVE EVOLUTION IN THE MOUTH OF THE COLUMBIA RIVER

A. INTRODUCTION

Tidal inlets and river mouths can present a significant hazard to navigation where extreme waves may develop as waves interact with complicated shoal systems and strong ebb tidal jets. Waves that interact with currents and bathymetry have been studied independently. However, due to the complications of making measurements in such dynamic regions, little is known of the combined effects on the spatial wave evolution.

As ocean waves transit regions with variable bathymetry and interact with strong opposing currents, they can undergo radical changes in their physical properties. The directions change due to refraction, wave heights increase as the group speed slows, and the waves can dramatically steepen against the current. In stationary conditions, the presence of a current changes the linear dispersion relation to $\omega = \mathbf{U} \cdot \mathbf{k} + \left(g|\mathbf{k}|\tanh\left(|\mathbf{k}|h\right) \right)^{\frac{1}{2}}$ where $\mathbf{k}$ is the wavenumber vector, g is gravity and the absolute frequency, ω, is conserved. If the local current, $\mathbf{U}$, and depth h are assumed to vary gradually over many wavelengths (Bretherton and Garrett 1968), it follows that in a framework that moves with the medium, the relative frequency, $\sigma = \left(g|\mathbf{k}|\tanh\left(|\mathbf{k}|h\right) \right)^{\frac{1}{2}}$, experiences a Doppler shift, $\sigma = \omega - \mathbf{U} \cdot \mathbf{k}$. The wavenumber vector, $\mathbf{k}$, varies spatially as well.

Jonsson (1990) provides a detailed overview of the dynamic and kinematic effects of wave-current interaction. The influence of currents on wave kinematics (relative phase velocity and wavenumber) is highly dependent on the strength and shear of the current and the angle at which the waves approach. Variations in phase velocity result in refraction of the waves that can be described using geometric optics theory that describes a ray path normal to a plane wave, which bends in response to lateral changes in phase speed (Jonsson 1990; Holthuijsen and Tolman 1991). When the waves oppose a strong current, the reduction in group velocity and an increase in relative frequency causes an

19

increase in wave height, which is accompanied by a decrease in wavelength that leads to a dramatic steepening of the wave. These effects are described by the wave action balance equation (eq. 1). From the linear dispersion relation, it can be shown that in extreme conditions where the waves directly oppose the current, blocking can occur when the relative group speed, $c_g = \dfrac{\partial \sigma}{\partial k}$ equals the opposing current speed, U. The frequency at which this occurs is known as the blocking frequency in deep water given by, $f_{bl} = \dfrac{g}{4\pi U}$. Wave energy at frequencies greater than f_{bl} can no longer propagate. Drastic changes in the wave conditions occur in blocking regions as the strong nonlinearity of waves breaking results in energy transfers to higher and lower frequencies of which only the lower frequency wave groups can propagate against the current (Lai et al. 1989; Chawla and Kirby 2002; Bascheck et al. 2006).

Wave-current interaction in a strongly sheared current can yield extreme wave conditions owing to wave amplification in caustics (rays crossing) and the subsequent wave turning into the current and evolving into steep breaking waves. These effects were observed as waves from the southern ocean interact with the strong Agulhus current south of the African Cape where the Agulhas current can exceed 2 m s^{-1} (Irvine and Tilley 1988). Similar conditions develop in the Gulf Stream when waves oppose the strong current (Holthuisen and Tolman 1991). Laboratory experiments suggest that enhanced wave conditions can occur in these situations particularly when wave-current interaction results in refractive focusing (Lai et al. 1989). Further, Chawla and Kirby (2002) confirmed findings in Lai et al. (1989) that breaking in response to currents is not saturated as is found in depth-limited breaking (Battjes and Janssen 1978) and that a down shift in the spectral energy occurs as the waves spill into the current. Additional observations from field studies (Wolf and Prandle 1999; Rusu et al. 2011; Van der Westhuysen 2012; and Dodet et al. 2013) outline the importance of wave-current interaction on wave predictions, but consist of limited observations that were made using fixed instruments.

In tidal inlets and river mouths where complicated wave refraction patterns result from the interaction with ebb tidal shoal systems, observations are extremely limited owing to the inherent difficulties in placing moored instruments in strong currents, large waves, and shipping lanes (Thomson 2012; Elias et al. 2012; and Pearman et al. 2014). In regions with a shoal system containing an elevated lens-shaped bathymetric feature, a focal zone, or caustic, develops in response to rays converging as waves refract toward shallower depths (i.e. regions with slower group speeds) (Vincent and Brigg, 1989; Smit and Janssen, 2013). It has been theorized that nonlinear instabilities can result in extreme waves in these caustics (Janssen and Herbers 2009). The location of the caustic is highly dependent on the offshore wave direction, which makes observing these phenomena with traditional moored (Eulerian) sensors difficult.

The mouth of the Columbia River (MCR), known as the 'Graveyard of the Pacific (Oregon State Parks), is one of the most dynamic wave environments in the world. It has claimed approximately 2000 ships since 1792, and serves as an ideal natural laboratory for measuring the effects of a complicated shoal system and strong wave-opposing current. Lai and Delisi (2010) used RADAR observations to determine that a large degree of spatial variability exists in the swell waves in the offshore approaches to the MCR. A field study called the Mega-Transect Experiment (MGT) that was conducted by the United States Army Corps of Engineers (USACE) in collaboration with the United States Geological Service (USGS) during the summer of 2005 designed to assess model skill in the region showed that wave current interactions are very important as wave heights nearly doubled at a station over the bar (Elias et al. 2012). However, a detailed spatial analysis of the physical mechanisms that affect specific frequency band evolution does not exist.

In this research, a Lagrangian sensing strategy is employed in which a large number of recently developed drifters are deployed on the peak of the ebb tidal current and allowed to drift through the most energetic wave regions. The spatial coverage of *in situ* observations that results is not practical using traditional Eulerian (moored) sensing techniques (Herbers et al. 2012, Thomson 2012, and Pearman et al. 2014).

This chapter begins with a description of the field experiment in Section B, and the analysis method is described in Section C. The opposing wave-current case study is presented in Section D, followed by a comparison of the observations with SWAN predictions in Section E. Finally, the extreme wave observations are discussed in Section F, followed by a summary in Section G.

B. FIELD EXPERIMENT

1. Field Site

The mouth of the Columbia River represents the interface between a massive river system and the Pacific Ocean (Figure 13). To reduce the maintenance requirements for the navigation channel and reduce the transit risk across the bar, the construction of the three-jetty system was completed in 1939 (Figure 13). A jet-like current develops between the jetties as the ebb tide couples with the natural discharge of the Columbia River that approaches 8000 m^3 s^{-1} (USGS). Large volumes of sediment are deposited as the strong current sculpts the complicated shoal system that is known to mariners as "the Bar". During our deployment, the offshore H_s was 1.75 m and the dominant offshore waves were from the west-northwest at 14 seconds (Figure 14) with secondary waves from the west-northwest at 10 seconds and a long period (18 seconds) south swell. In addition to the swell, a weak locally generated 5-second period wind-sea from the west-northwest was present.

2. Wave Resolving Drifters

The three slightly different Wave Resolving Drifters (WRDs) used to measure the currents and waves in this research (Figure 15) are equipped with GPS data loggers that measure position and horizontal orbital velocities of the swell waves. Accelerometers measure vertical accelerations of the higher frequency wind-waves.

The first type of WRD, WRD-A has a 1 Hz GPS data logger that records u and v Doppler velocity data and positional data and an accelerometer tethered beneath the surface drifter (for details see McIntyre, 2013 and Pearman et al. 2014). In the second WRD design, WRD-B, an acrylic shell houses the same GPS data logger and a more

sophisticated Inertial Motion Unit (IMU) accelerometer package (see Portell, 2013 for details). Both WRD-A and WRD-B are also equipped with a GPS RF transmitter for real-time tracking. The final WRD design, WRD-J is more sophisticated with a 5 Hz GPS, an IMU accelerometer and an iridium transmitter for over the horizon tracking, all housed in the acrylic shell. The WRD are spherical and have an immersion resonance frequency greater than 1 Hz that is outside the range of interest for this research. Each individual sensor has its own time keeping method so common time stamps for each drifter were arrived at using the GPS time on each WRD following the methods outlined in Herbers et al. (2012) and Pearman et al. (2014).

3. Drifter Deployment

This field experiment consisted of many deployments; however, this research will focus on one major deployment in which the offshore conditions resulted in the most dramatic wave evolution. The deployment of 30 WRD was conducted on June 08, 2013 during the peak ebb tidal current from R/V Point Sur as it maintained station centered on the ebb tidal jet in the Columbia River estuary (Figure 13), starting at 1220 UTC near the peak ebb tidal current (predicted to occur at 1322 UTC, NOAA Tide Tables).

The 30 WRD were deployed at 20-second intervals resulting in approximately 60 m spread between drifters. As the WRD exited between the jetties and transited the bar with the ebb tidal jet exceeding velocities of 3 m s^{-1}, they expanded laterally relative to the mean drift direction but remained clustered along-track (east-west) following the MCR alluvial plume (see Figure 16).

C. LAGRANGIAN ANALYSIS

1. Drifter Analysis

The drifter time series are nonstationary along the long drift track owing to the Lagrangian nature of the measurements as the drifters move with the strong current through the spatially inhomogeneous wave field. Therefore, two approaches were taken to the spectral analysis. First, the auto- and cross- spectral estimates were computed for relatively short segments (204.8-seconds) of the GPS and accelerometer time series

applying a Hamming window. The auto spectra of GPS and accelerometer were combined to form a surface height spectrum $E(f)$ using the horizontal GPS velocity observations in the swell range 0.03 Hz – 0.15 Hz and vertical accelerations in the wind-sea range 0.25 Hz – 1.0 Hz. In the transition range of 0.15 Hz – 0.25 Hz, a weighted average of the two sensors was used where the GPS (accelerometer) weighting was varied linearly from 1(0) at 0.15 Hz to 0(1) at 0.25. Linear theory transfer functions (Table 2) were applied to convert velocity and acceleration spectra to surface height spectra (see Pearman et al., 2014 for details). From these raw surface height spectra the significant wave height, $H_s = 4\left(\int_{0.03\,\text{Hz}}^{1.0\,\text{Hz}} E(f)df\right)^{\frac{1}{2}}$, was evaluated (following Pearman et al., 2014), and these were ensemble averaged across drifters on a grid with spacing of 50 m (north) x 100 m (east) chosen based on the lateral divergence (north-south) of the various drift trajectories. To estimate accurate wave spectra that resolve the multi-modal wave field, seven regions of similar characteristics were selected starting with the Bar (B) and moving outside (inside) of the bar where O1 (I1) is closest and O3 (I3) is the farthest (Figures 16, 17). For each drifter, the entire time series during passage of a given region was used to estimate the surface height spectrum, $E(f)$ with FFT window lengths of 2048 samples (at 10 Hz) and 50% overlap yielding a frequency resolution of 0.0049 Hz. The spectrum from each drifter in a given zone is then ensemble averaged and a single more statistically stable ensemble spectrum is presented (Figure 18, discussed below). Additionally, histograms of H_s in each zone are used to identify deviations from the offshore distribution that can potentially indicate rogue wave development (Figure 19, discussed below).

2. Ray-Trajectories

Rays based on the offshore wave conditions were traced across the domain to assist in analysis of the wave field and, in particular, the evolution of those waves dominant in the spectrum (see Figure 20). Geometric optics theory suggests that in a slowly varying medium, a plane wave of a particular frequency will follow the wavenumber vector $\mathbf{k}(k_x, k_y)$ that varies slowly in response to refraction by depth and

24

current variations. The wave number magnitude k is calculated from the dispersion relation based on the relative frequency σ and local depth. The rays are traced with a simple iterative scheme to adjust σ for the Doppler shift $\mathbf{k} \cdot \mathbf{U}$ that depends on the angle of the local plane wave to the local current from the modeled flow field described in Section E. In each iteration the ray equation:

$$\frac{d\phi}{ds} = \frac{1}{k_0}\left(-\sin(\phi)\frac{\partial k}{\partial x} + \cos(\phi)\frac{\partial k}{\partial y}\right) \tag{3}$$

is solved where $\dfrac{\partial k}{\partial x}, \dfrac{\partial k}{\partial y}$ are calculated on a 50 m x 50 m grid. The starting points for the rays are selected at an offshore location such that the bathymetry and currents do not influence the waves. The ray spacing is constant along the outer edge of the grid (50 m) and each ray is traced using 10 m increments along the ray trajectory, s, and analyzing using ancillary relations, $\dfrac{dx}{ds} = \cos\phi$, $\dfrac{dy}{ds} = \sin\phi$.

The predicted bend in response to the phase speed variations along the wave crest induced by the variable bathymetry and sheared currents. The convergence (divergence) of the rays that results indicates areas of increasing (decreasing) energy. When the refraction is strong enough, a caustic (rays crossing) can result, and when current shear is strong the rays can become trapped and refract back and forth across the current in a snake-like pattern (Mei 1983).

D.   CASE STUDY: WAVES OPPOSING CURRENT

The offshore wave conditions are somewhat complex; however, the following analysis will focus on the dominant west-northwest swell (14-second) and the 5-second wind-sea that are affected in different ways by the shoal and tidal currents that exceed 3 $m\,s^{-1}$ (Figure 16). This approach capitalizes on the dense spatial coverage of H_s to obtain a synoptic view of the wave height variability across the mouth of the Columbia River (Figure 17). Additionally wave spectral estimates in the seven selected zones (Figure 18) are presented to provide a more detailed analysis of the transformation of the swell and sea components. The wave height and spectral

25

estimates are combined with ray computations to identify the bottom and current features that are primarily responsible for the wave variability.

1.   Dominant Wave Evolution

The offshore H_s are relatively homogenous with a mean H_s near 2.5 m and a standard deviation in the distribution of about 0.9 m (Figure 19). The peak of the spectrum (0.065 Hz) in Zone O3 is dominated by a 14-second swell where the directional spread is at a minimum and the direction is from the west-northwest (Figure 18). The straight and evenly spaced rays indicate little bathymetric or current influence (Figure 20) until the lens shaped shoal in the NE corner of Zone O2 where the rays refract and converge in a well-defined caustic. The resulting cross-wave patterns are evident in the nearby doubling of the directional spread (Figure 18). The spread in H_s estimates remains near constant although the mean increases to 2.8 m. The region of increased H_s in the center of the zone (Figure 17) closely coincides with the core of the ebb tidal jet (Figure 16) suggesting some shoaling (i.e. decreasing group speed) in response to the opposing current ($> 2.5\,\mathrm{m\,s}^{-1}$) may also contribute to the enhanced wave heights. This wave-current interaction is also evident in the Doppler shift of the spectral peak to 0.083 Hz.

In Zone O1 the elevated peak in the spectrum is further Doppler shifted (Figure 18) as the opposing current reaches 3 $\mathrm{m\,s}^{-1}$ (Figure 16), and a focused line of elevated H_s oriented from the west-northwest to the east-southeast develops (Figure 17) that closely corresponds to the caustic that forms as the rays converge down wave of the lens shaped shoal located in Zone O2 (Figure 20). The enhanced H_s of 3.7 m are almost double the ~ 2 m H_s values observed to the north and south of the focusing region. Similar enhancements were identified in laboratory experiments (Vincent and Briggs, 1989) where narrow band (in a directional sense) waves were found to nearly double in height in the caustics.

In Zone B, on the bar, the wave heights are further enhanced ($H_s > 5$ m), with the largest waves in the northern portion of this zone in contrast to the ~ 3 m observed in southern portion. (See also the significantly greater spread in the distribution, Figure 19)

The sharp gradient of wave heights over very short distances (Figure 17) suggests that these enhanced waves are the result of local physical processes. The increase in energy appears to be concentrated at the peak of the spectrum (Figure 18). However, the rays from the dominant 280 degrees offshore direction pass to the south of the region of maximum wave height. The refraction effects are sensitive to the incident wave direction, and therefore, it is important to consider the directional spread about the mean wave direction. The directional spread is 15 degrees near the spectral peak (Figure 18, bottom), so waves approach the shoal from a range of angles around the dominant offshore direction. Rays at the same offshore frequency from 270 degrees (Figure 21) refract around the south side of the shoal and are indeed concentrated in this region of enhanced H_s well down-wave from the caustic providing a possible explanation for this pronounced enhancement.

Behind the bar in Zone I1 the enhanced H_s are no longer evident, which is consistent with the reduction in the peak of the spectrum (Figure 18). The persistent strong current and lack of a noticeable Doppler shift suggests that the notable decrease in H_s on the central portion of the zone can be partially attributed to the increased water depth (unshoaling), but more importantly, the ray trajectories in this deeper area surrounded by shoals indicate an energy divergence similar to observations in other inlet studies (Elias et al. 2012; Dodet et al. 2012; Pearman et al. 2014).

Zone I2 is well within the inlet, however, H_s remains elevated near 3 m (Figure 17), and the peak shifts further to a higher frequency (Figure 18). The overall pattern shows ray divergence toward the sides of the inlet, and a concentration of the rays in this region (Figures 20 and 21) turns into the current suggesting waves in this band continue to shoal into the strong current (>3 m s^{-1}). The change in the mean wave direction from southwest to west and low directional spread (Figure 18) are consistent with this ray pattern.

By the time the dominant rays reach the eastern portion of Zone I3 the divergence of the wave energy results in a dramatic decrease in spectral levels at the dominant swell peak (Figure 18). The decrease in H_s to about 1 m (Figure 17) is similar to what was

27

observed in SF Bay (Pearman et al., 2014). However, it occurs much farther into the inlet in MCR where the currents are significantly stronger (about a factor of 2) indicating that wave focusing on the current, which counteracts energy divergence caused by depth-induced refraction, is more important in the MCR than in SF Bay.

2.　Wind-wave Band

Interpretation of the evolution of the wind-wave band is complicated by the directional spread, which is much larger than at the dominant peak (Figure 18). Laboratory experiments (Vincent and Briggs, 1989) show that for broadband (directional) waves the increase in wave heights on opposing currents is much less dramatic than narrow-band waves. Therefore, when calculating the blocking frequency (the frequency at which waves will no longer propagate into an opposing current) using the linear dispersion relation, $f_{bl} = \dfrac{g}{4\pi U \cos\alpha}$, where α is the difference in angle between $-\mathbf{U}$ and $\mathbf{k}$, it is important to note that only the waves for which α is sufficiently small will actually be blocked (e.g. f_{bl} is twice as large for an $\alpha = 60°$ compared with the pure opposing $\alpha = 0$ case). Thus, when a directionally broad wave field encounters a current jet, the small α components are amplified as they refract and shoal into the current, whereas the large α components merely cross the jet. Bathymetry effects are negligible as is clear in the comparison of the rays with currents (Figure 22) and without currents (Figure 23). The following analysis progresses from the offshore Zone O3 to inside of the bar to in Zone I3.

The relatively broad spectral peak near 0.2 Hz in Zone O3 is amplified progressively until it reaches a maximum in Zone B where the mean velocity is 3 m s^{-1} and f_{bl} = 0.27 Hz for $\alpha = 0$. The considerable convergence of the rays, particularly in the eastern portion of the zone, indicates that the waves are becoming highly focused on the current and thus refraction (in addition to shoaling) may contribute to the increase in energy. The spectrum decreases slightly in Zone I1 before increasing in Zone I2 where the rays are now directly opposing the current, and the directional spread has reduced from 30 degrees to 20 degrees. The dramatic reduction in energy in Zone I3 is indicative

of blocking of those waves angled into the current in Zone I2 where the mean velocity is 3.3 m s^{-1} and the $f_{bl} = 0.23$ Hz for $\alpha = 0$. Additionally, the ray trajectories indicate that waves from the mean offshore direction become trapped (refracting back and forth across the jet as described in Mei 1983) on the current which by-passed Zone I3 almost entirely (Figure 22).

E.   SWAN COMPARISON

The wave action balance equation at the core of phase averaged models like SWAN has been shown to predict, with reasonable skill, the evolving wave statistics over slowly varying bathymetry and in the presence of currents (Booij et al. 1999 and Ris et al. 1999).   However, phase-averaged models tend to generally over-predict H_s in strong opposing currents (Van der Westhuysen 2007 and 2012) and to miss the peaks in regions of highly focused wave energy (Cavaleri 2009; Janssen and Herbers 2009; Smit and Janssen 2013). The measurements used in prior field evaluations of SWAN were mostly Eulerian in nature, relatively sparse and do not cover wave evolution in extreme currents and through caustic regions.

In this research SWAN was one-way coupled with velocity output from the circulation model, SELFE (semi-implicit Eulerian-Lagrangian finite-element model). SELFE is a 4-dimensional baroclinic circulation model that has been designed for use in the MCR region (Zhang and Baptista 2008). SELFE solves the 3D nonlinear shallow-water equations for free surface elevation and 3D velocity-salinity-temperature with hydrostatic and Boussinesq approximations and transport equations for salt and heat. The external forcing consists of 4-semidurnal tidal constituents along the offshore boundary and the discharge of the Columbia River at a location sufficiently upstream to be beyond the maximum salt-water intrusion, using measurements gathered as part of from Center of Coastal Margin Observation and Prediction (CMOP) program. (SELFE model output is downloadable from the CMOP website: http://www.stccmop.org)

The SWAN model was implemented on a variable resolution grid that uses ~100 m grid spacing offshore and 10 m in regions where bathymetry (from the NOAA bathymetry database) showed rapid horizontal variability. The wind and wave forcing

were taken from observations made at NOAA buoy 46089 located 160 km offshore (for details on source term selection and set up see Pearman et al. 2014). Multiple SWAN simulations in which source terms were individually disabled were conducted to evaluate the dominant physical mechanisms influencing the SWAN predictions (Table 1). The H_s from the SWAN simulations (Figure 24) evaluated here are collocated in space and time with WRD measurements (Figure 17), and the SWAN spectra (Figure 25) are selected at a grid point close to the center of the each zone at a time consistent with the drifter observations from that zone.

The general wave pattern predicted by the SWAN simulation (Figure 24) compares rather well with the WRD estimates (Figure 17). However, the SWAN predictions tend to be biased high, particularly in Zones I2 and I3 where the currents are strongest (Figure 26). Of particular interest is the clear jump in the peak of the spectrum moving from Zone O2 to Zone O1 in response to the caustic that forms down-wave from the lens-shaped shoal (Figure 13). The location of the elevated H_s in the SWAN simulation (Figure 12) coincides with the location where the WRD observe amplification, but show about a +0.5 m high bias. The elevated energy level at the peak of the spectrum when compared to the WRD in this zone may be due to the ensemble averaging of the WRD spectrum calculated within this zone versus the single point spectrum of SWAN that falls within the caustic in the ray trajectories (Figure 21).

The region of extreme H_s that was observed in the WRD measurements in Zone B (Figure 17) is evident in the SWAN predictions slightly further east (on the edge of Zone B and Zone I1). However, the enhanced H_s are under predicted by as much as 3.5 m or 50%, and the high degree of spatial variability in the WRD measurements when compared to the smooth SWAN predictions demonstrate that SWAN does not effectively capture this sharp region of very enhanced waves (Figure 26). While the peak of the spectrum remains elevated in this zone (Figure 25) it is fairly close to the previous zone and does not show the dramatic increase in the dominant spectral peak that is evident in the WRD spectrum (Figure 18). Rather the limited increase in H_s results from elevated energy levels at higher frequencies in response to the strong current (~ 3 m s^{-1}), which is

confirmed by the much lower H_s from the SWAN simulation in which the currents are disabled (Figures 26 and 27).

The next region of elevated wave heights falls in Zone I2 where SWAN predicts H_s in excess of 4m compared to the observed wave heights of less than 3 m (Figure 24). The SWAN simulation with the currents disabled (Figure 27) indicates that the currents are responsible for the high bias, which is confirmed in the 1-1 comparison (Figure 26). The spectrum in this zone (Figure 25) shows that the elevated energy levels at frequencies higher than the spectral peak and provides a clear example of the model under-dissipating wave energy on strong opposing currents.

F.   EXTREME WAVES

Whereas much of the spatial wave variability observed with the WRD array is at least qualitatively consistent with expected bottom- and current- induced shoaling and refraction effects, the extreme waves observed in Zone B warrant more discussion. The dramatic changes in H_s that occur on relatively small spatial scales over the MCR Bar (zone B) are highly localized in the central and northern portion of the zone (Figure 17). Multiple drifters experienced enhanced wave development in a very focused region that is well down-wave from the refraction caustic (Figure 28). The waves nearly triple in H_s over a distance of less than a few wavelengths. Comparison of the spectra that have been ensemble averaged over enhanced (H_s >= 4.5 m) and unenhanced (H_s <4.5 m) individual drifter time series shows that the most significant amplification in the spectrum occurs at the dominant peak (Figure 30).

The waves become focused on the combination of the ridge shaped shoal and the opposing current and the directional spread is 7 degrees narrower at the spectral peak in the enhanced spectrum than it is in the unenhanced spectrum (Figure 30). A clear negative correlation between H_s and directional spread (Figure 31) supports the hypothesis that refractive focusing causes the anomalously larger waves.

To further investigate the behavior of these waves, it is helpful to do so in the time domain. However, as outlined earlier, the accelerometer (direct measure of vertical

motions) is inaccurate in the swell band where double integration of the accelerations to arrive at displacements results in an O(4) amplification of the noise in the swell band (see Appendix A). However, in a narrow band linear wave field the horizontal velocity component in the dominant wave direction is proportional to the vertical wave height profile with a transfer function that equals $\frac{gk}{\sigma}$ (Herbers et al. 2012). Therefore, the horizontal orbital motions in the time domain provide insight into the wave evolution (Figure 31). The drifter shown here that records the largest waves is moving from right to left, and thus the evolution of waves traveling from left to right is shown in reverse. Between times 12:40 and 12:34 the orbital velocities are unremarkable with the appearance of normally shaped wave groups and variations $\pm 1\,\mathrm{m\,s^{-1}}$. As the drifter passes through the amplified wave group (near time 12:34-12:32), the orbital velocities become so extreme as to occasionally exceed the mean drift velocity of 3 $\mathrm{m\,s^{-1}}$ and a complete reversal of flow results. These enhanced orbital velocities are more than twice those measured before and after the extreme wave event. The highly localized nature of these enhanced velocities suggests rogue wave development.

The rays in this region are within a few degrees of the primary current direction (Figure 28), conditions that were found to be ideal in deep water investigations of rogue wave development discussed in the introduction. While the lens shaped shoal is critical in setting up the conditions for rogue wave development, the actual extreme waves occur well down wave from the dramatic caustic as the waves become focused in response to the ridge shaped shoal and the strong current. This indicates that the development is in response to nonlinear instabilities that steepen and enhance the waves in this region, similar to what was modeled in the idealized conditions by Janssen and Herbers (2009).

G.   SUMMARY

The complicated bathymetry that is sculpted by the strong outflow from the Columbia River creates a spatially variable wave field that is difficult to measure using traditional moored instruments. The lens-shaped shoal at the leading edge of the bar system is the dominant forcing feature in the region that focuses swell waves through a

caustic as they refract toward shallow water. The waves then encounter a complicated bar system that has a ridge shaped shoal extending out the lens and a shallow bar that crosses the channel. The effects of this irregular bathymetry and the combined tidal and river flow that can exceed 4 m s^{-1} result in localized extreme wave conditions.

To measure this wave evolution 30 Wave Resolving Drifters (WRD) were deployed on the peak ebb tide from inside the river mouth and allowed to drift through the opposing wave field with the current and recovered at the seaward edge of the river plume several kilometers offshore. Because of the exceedingly strong current and general spatial inhomogeneity of the wave field through which the WRD passed, relatively short segments were used to estimate significant wave height, H_s, which were then ensemble averaged on a spatial grid in order to obtain a robust synoptic estimate of the wave field variability. Zones of similar wave characteristics were identified and spectra were calculated from the time series of the drifter measurements within the zone and ensemble averaged to resolve the spectral properties of the complex multi-modal wave field.

The offshore wave conditions on 8 June 2013 consisted of a dominant 14-second swell and a weak 5-second wind-sea both arriving from the west-northwest. The wind-sea was highly influenced by the strong ebb tidal jet exiting the channel. It was shown using rays that the waves appear to become trapped on the strong current. SWAN-SELFE coupled model simulations were compared with these observations and it was found that SWAN simulations tend to under-dissipate the high frequency waves as they shoal and break onto the strong current and generally carry too much energy in the higher frequencies well into river.

The dominant west-northwest 14-second period waves refract on the lens shaped shoal at the outer approaches to the MCR ebb tidal shoal region and form a caustic on the eastern side. The wave heights are amplified in the caustic region largely due to the refractive effects. However, the rays that refract around the southern part of the lens remain tightly spaced as they exit the caustic and oppose the current while moving along a ridge shaped shoal that extends seaward from the north jetty. Extreme waves were observed along these rays, and although there is enhancement in the high-frequency

33

portion of the spectrum, the dominant increase in energy is within the swell peak. The observed WRD orbital velocities in the region show an abrupt doubling in intensity indicating rogue wave development.

A coupled SWAN-SELFE simulation shows a slight wave enhancement in the region where large waves were observed. However, the increased energy levels predicted by SWAN are in the higher-frequency portion of the spectrum (away from the swell peak) indicating the model does not adequately dissipate waves that are blocked by the opposing current. The lack of enhancement at the spectral peak in SWAN supports the hypothesis that the rogue wave development is largely due to nonlinear instabilities that develop down wave from the caustic rather than from purely refractive effects.

IV.   SUMMARY AND FUTURE WORK

A.   SUMMARY

The two chapters contained herein outline the development and application of new drifters that were engineered for use in tidal inlets and estuaries. The wave resolving drifters (WRD) were found to produce results comparable with more sophisticated and expensive 'state of the art' three axis wave buoys. The deployment and of the WRD in large numbers coupled with a methodology based on ensemble statistics of the non-stationary time series facilitated evaluation of wave evolution at a spatial density that was not achievable using traditional (Eulerian) *in situ* measurement strategies alone.

The addition of an accelerometer package removes the 180-degree direction ambiguity that was evident in earlier GPS-only drifter designs. The accelerometer also provides direct vertical measurements of higher frequency wind waves in the spectral tail that is not possible using GPS that are less responsive at high frequencies. Ensemble averaging wave spectra over many drifters allowed us to resolve the complex inhomogeneous and multi-modal wave fields. These spectra were used in conjunction with ray computations to provide insight into the frequency-specific evolution of a wave field.

The physical mechanisms responsible for the variable wave field in the San Francisco Bight were analyzed with coupled Delft3D FLOW and SWAN simulations. It was shown that refraction over the bifurcated shoal system of the Four Fathom Bank and the South Bar is the dominant mechanism that controls the spatial variability of the swell waves. In contrast, the strong ebb tidal jet controls the wind wave band. The shape of the inlet results in divergent rays at the both the swell and wind wave frequencies, and thus wave energy entering the channel is limited.

The conditions in the Mouth of the Columbia River (MCR) were challenging. Both wave-bottom and wave-current interaction processes contributed to the wave evolution similar to what was observed in the San Francisco Bight. However, unlike the San Francisco Bight, in the MCR the wind waves get trapped on the current and penetrate

well into the river mouth. Additionally, the longer period west swell is focused sharply on the lens-shaped shoal outside of the jetties forming a well-defined caustic. The largest waves were observed well down-wave from the caustic indicating likely rogue wave development in response to nonlinear instabilities of waves amplified by wave-bottom and wave current interaction. This experiment confirmed that the phase-averaged models used operationally by the Navy tend to under-dissipate wave energy in strongly opposing currents, but it also highlighted that these models do not resolve and, in fact, drastically under-predict extreme wave development in caustic regions.

B.   FUTURE WORK

The analysis of these experiments is ongoing. The additional deployments that were conducted in the San Francisco Bay provide an opportunity to investigate how waves develop in these regions under various offshore conditions. On February 15, 2012, the drifters followed the complicated current pattern in which some of the drifters went offshore over the bar, but one WRD drifted north over the Four Fathom Bank, was trapped in an eddy, crossed the bank again and eventually entered and exited the surf zone. Another drifter exited the channel and did not cross the South Bar, before the current reversed and eventually drifted along the coast of Ocean Beach. Several large deployments were conducted in October of 2012 to observe wave evolution across the bar in more detail.

Two additional major deployments were conducted at the Mouth of the Columbia River. The first was on May 27, 2013, when there was a south swell and the winds were offshore. The preliminary analysis of the 30 WRD time series and evolution of the spectrum indicate fetch limited wave growth on a strong following current. In the second major deployment on May 29, 2013, a total of 47 WRD were deployed and allowed to drift approximately 18 km north following the ebb tidal plume. On both of these days extreme wave development was not observed, which indicates that the offshore wave conditions may be an important factor in establishing the focusing that leads to rogue wave development.

C. NAVY RELEVANCE

Recent advances in GPS and Inertial Measurement Units (IMU) technology have significantly reduced the total cost for the components used in these wave-resolving drifters to around $1000. The processing that was done here could be completed onboard, thus allowing for spectra and bulk wave statistics (a relatively small data set) to be transmitted in near real-time. Further, the error in the IMU measurements is significantly reduced when the 3-axis magnetometer, 3-Axis gyro and 3-axis accelerometer combination is used to transform the body frame accelerations into linear accelerations in the earth reference frame (see Portell, 2013). It follows that as the technology (software and hardware) improves, the double integration from accelerations to displacements in the time domain will facilitate direct investigation of individual wave parameters (slope, height, and length) that are likely important in understanding rogue wave development.

Drifters like these can also be used to fill in the gaps in regions where the existing observational network is limited, or more detailed spatial resolution is necessary for the validation and improvement of numerical model predictions. While a detailed model validation is not the focus of this research, it clearly shows that these drifters are useful in identifying the weaknesses in the phase-averaged models that are currently used by the U.S. Navy to make predictions in shallow water regions. Current literature that identifies the tendency for SWAN to over-predict the wave heights in regions with waves opposing strong currents is limited by the Eulerian observations that were used. However, the comparison in this research, made possible by these spatially dense Lagrangian drifter observations, shows that SWAN also severely under predicts the peaks of extreme wave amplification in these conditions. An assumption that waves are over predicted can result in elevated risk to the mission and an increased risk to forces resulting from the very high probability that operators will experience wave conditions that well exceed their operational limits. The improved understanding resulting from this research can help eliminate this worst-case operational risk management scenario.

THIS PAGE LEFT BLANK INTENTIONALLY

APPENDIX A. VERTICAL DISPLACEMENT SPECTRA AND BULK STATISTICS

We evaluated the new WRD performance through comparison with measurements from a Datawell Wave Rider DWR-G4 directional buoy, which derives three-dimensional velocity from the Doppler shift estimates of the raw GPS L1 carrier signal (similar to the GT-31 GPS). In the internal processing these velocities are integrated to produce three-dimensional displacement time series. The Datawell GPS-based measurements have been carefully validated against earlier generation Datawell buoys with accelerometers, compass and tilt sensors (de Vries et al., 2003, Herbers et al., 2012) and thus can be considered a reliable "ground truth" for the WRD measurements.

We selected a deep-water site (1700 m) well offshore (40 km) to reduce effects from coastal sheltering, shoaling and refraction on the wave statistics. A well-developed wind sea in a nearly constant northwest wind of ~15 $m\,s^{-1}$ persisted throughout the period over which the measurements were made. Three WRDs were deployed alongside the Datawell. The largest separation distance between the Datawell and the WRDs during the experiment was 2.1 km, which is small compared with the typical O(100 km) scale of variability in open ocean wave conditions. Therefore, the statistics of the wave field measured by the WRD and the Datawell buoy can be assumed to be the same.

A. ACCELEROMETER PERFORMANCE

The X6-2 sensor was tethered beneath the drifter to decouple the sensor from the pitch and roll motions of the surface buoy in steep waves. However, while the pitch and roll effects are effectively dampened, occasional steep, near-breaking waves may cause large tilt angles of the ballast chain and sensor package that cannot be quantified without a tilt sensor (gyroscope or magnetometer). These uncorrected motions are evident in occasional large acceleration spikes that cause a small bias (~5-10 %) in wave height estimates (McIntyre, 2013).

To quantify the order of magnitude of the errors introduced in vertical acceleration measurements by the instrument tilt motions, we consider the idealized case

of an accelerometer package rigidly attached to a surface-following buoy. As the buoy pitches and rolls in response to the sea surface motion, errors are introduced in the vertical acceleration measurement a_z by both the horizontal acceleration components a_x, a_y and variations in the static gravity force component normal to the sea surface. These latter variations have the same time scale as the wave-induced surface height fluctuations and thus are of particular concern here. For small values of the surface slopes η_x and η_y the error (ε) in the measured vertical acceleration can be expressed as:

$$\varepsilon = a_x \eta_x + a_y \eta_y - \frac{1}{2}\left(\eta_x^2 + \eta_y^2\right)\left(a_z + g\right) \tag{A1}$$

In the linear wave theory approximation $|a_z| = g$ and at the surface

$$a_x = -g\eta_x, \ a_y = -g\eta_y \tag{A2a, b}$$

and thus Eq. (A1) reduces to

$$\varepsilon = \frac{g}{2}\left(\eta_x^2 + \eta_y^2\right) . \tag{A3}$$

This analysis shows that the tilt error in the vertical acceleration measurement is comparable to second order non-linear effects and thus can be formally neglected in the linear approximation. However, the quadratic slope-squared term in Eq. (A3) affects the measured accelerations not at the primary surface wave frequencies, but at the sum and difference frequencies of pairs of wave components. Thus in mixed swell-sea wave fields, that are commonly observed in the ocean, the relatively steep wind wave slopes may degrade the acceleration measurements at lower swell frequencies where a_z is typically much smaller than g. This sensitivity is confirmed in the field test, which show a positive bias of about 10% in swell spectral levels from the accelerometer data (McIntyre, 2013). In contrast to the expected low signal-to-noise ratio at swell frequencies, the measured accelerations of steeper wind wave components that usually dominate the surface slope spectrum, are insensitive to this source of error. Hence the accelerometer complements the GPS sensor that is better suited to observing the longer period, lower steepness swell (Herbers et al., 2012).

B.   VERTICAL DISPLACEMENT SPECTRA

To obtain an accurate wave spectrum across the entire swell and wind wave bands, we form a composite spectrum using the GPS estimate below 0.15 Hz, the accelerometer estimate above 0.25 Hz, and a weighted average in between. The GPS (accelerometer) weighting was varied linearly from 1(0) at 0.15 Hz to 0(1) at 0.25 Hz. This composite wave spectrum produced the most statistically reliable estimates of H_s when compared to the Datawell results. The resulting WRD spectra are in excellent agreement with the Datawell spectra (Figure 2). Although ground truth was not available for direct comparison with the spectral tail, the spectrum rolls off as f^{-4}, which is in agreement with observations of equilibrium wind-wave spectra (Toba 1973; Phillips 1985; Battjes et al. 1987; Alves and Banner 2003). The merged spectral estimates of the significant wave heights $H_s \equiv 4E^{1/2}$ (with E the variance across the entire $0.05 - 1.0$ Hz range) were found to be less than 3% greater than those of the Datawell.

C.   SPATIAL AVERAGING ANALYSIS TECHNIQUE

The deep-water homogenous dataset was analyzed following the same procedures used in the inhomogenous tidal inlet region in order to demonstrate the accuracy of the ensemble averages of H_s estimates based on short record lengths and compared with results using a more standard 20 minute record length. As expected, the variance in H_s values estimated using the same short segment lengths (410 s) that were used in the tidal inlet analysis, 0.13 m^2, is larger than the 0.06 m^2 estimated from the standard 20-minute segment lengths. However, once the spatial and ensemble averaging is applied to the three drifters, the variance is reduced to less than 0.001 m^2.

THIS PAGE LEFT INTENTIONALLY BLANK

APPENDIX B. DIRECTIONAL ANALYSIS AND BULK STATISTICS

A.   DIRECTIONAL ANALYSIS

The direction θ is defined in a coordinate system with the x-axis pointing east and the y-axis pointing north ($\theta = 0$ for waves travelling from the west, $90°$ from the south). The lowest four Fourier moments of the directional distribution of wave energy $S(\theta)$ at each frequency can be expressed in terms of normalized cross-spectra (Long, 1980)

$$\begin{pmatrix} a_1 \\ b_1 \\ a_2 \\ b_2 \end{pmatrix} \equiv \int_0^{2\pi} \begin{pmatrix} \cos\theta \\ \sin\theta \\ \cos 2\theta \\ \sin 2\theta \end{pmatrix} S(\theta)d\theta = \begin{pmatrix} Q_{xz}/\sqrt{(E_{xx}+E_{yy})E_{zz}} \\ Q_{yz}/\sqrt{(E_{xx}+E_{yy})E_{zz}} \\ (E_{xx}-E_{yy})/(E_{xx}+E_{yy}) \\ 2C_{xy}/(E_{xx}+E_{yy}) \end{pmatrix}$$

(B1)

where C and Q are the co- and quadrature part of the cross-spectrum, respectively. Equation B1 applies to x, y, z displacements but can be adapted to velocity and/or acceleration measurements by using transfer functions based on linear wave theory (Table B1).

Estimates of $\bar{\theta}$ and σ_θ can be obtained from the first-order moments:

$$\tan(\bar{\theta}) \equiv \frac{b_1}{a_1}$$

(B2a)

$$\sigma_\theta \equiv \sqrt{2\left(1-\sqrt{a_1^2+b_1^2}\right)}$$

(B2b)

where $\bar{\theta}$, defined on a full circle, corresponds to the direction of the energy flux vector and σ_θ can be interpreted (in the limit of a narrow directional spectrum) as the standard deviation of $S(\theta)$.

Alternatively, the second-order estimates of $\bar{\theta}$ and σ_θ are given by:

$$\tan(2\bar{\theta}) \equiv \frac{b_2}{a_2}$$

(B3a)

$$\sigma_\theta \equiv \sqrt{\left(1 - \sqrt{a_2^2 + b_2^2}\right)/2} \qquad \text{(B3b)}$$

where $\bar\theta$, defined on a half circle, corresponds to the major axis of the horizontal wave orbital displacements and σ_θ describes the associated polarization (e.g. Herbers et al., 1999).

Estimates of $\bar\theta$ based on the second-order moments (B3a) are generally less useful than first-order estimates (B2a) because they suffer from a 180° ambiguity in the directional estimates. However, the second-order $\bar\theta$ and σ_θ (B3a, b) depend only on the horizontal measurements and thus provide a consistency check on the first-order estimates that use the vertical acceleration measurements and allow for comparing independent estimates based on GPS position and velocity data. The directional estimates from the WRDs are in fairly good agreement with the Datawell estimates (Figure 2). Additionally, the first order moments do indeed eliminate the 180-degree ambiguity that is evident in the second-order estimates the below spectral peak and near 0.3 Hz.

B.   BULK WAVE DIRECTIONAL PARAMETERS

In addition to the direction spectral estimates $\bar\theta(f)$ and $\bar\sigma(f)$, estimates of bulk wave parameters were obtained from short wave records to characterize wave conditions in the strongly inhomogeneous conditions of the San Francisco Bight. Energy-weighted bulk estimates of $\bar\theta$ and $\bar\sigma$ were obtained by integrating the auto- and cross-spectra in Eq. A1 over the swell-sea frequency range (0.05-0.3 Hz). The bulk directional estimates were found to be within 5 degrees of the Datawell estimates.

TABLES

SWAN	WIND	BOTTOM FRICTION	CURRENTS
Sim#1	On	On	On
Sim#2	Off	On	On
Sim#3	On	Off	On
Sim#4	On	On	Off

Table 1.   Summary of SWAN simulations in which various processes were disabled.

Displacement Spectra	E_{xx}	E_{yy}	E_{zz}	Q_{xz}	Q_{yz}	C_{xy}
WRD	$\dfrac{E_{uu}}{\omega^2}$	$\dfrac{E_{vv}}{\omega^2}$	$\dfrac{E_{aa}}{\omega^4}$	$\dfrac{C_{ua}}{-\omega^3}$	$\dfrac{C_{va}}{-\omega^3}$	$\dfrac{C_{uv}}{-\omega^2}$

Table 2.   Conversion of WRD auto- and cross spectra of vertical acceleration (a) and horizontal velocities (u,v) to equivalent displacement spectra using linear theory transfer functions.

THIS PAGE LEFT INTENTIONALLY BLANK

FIGURES
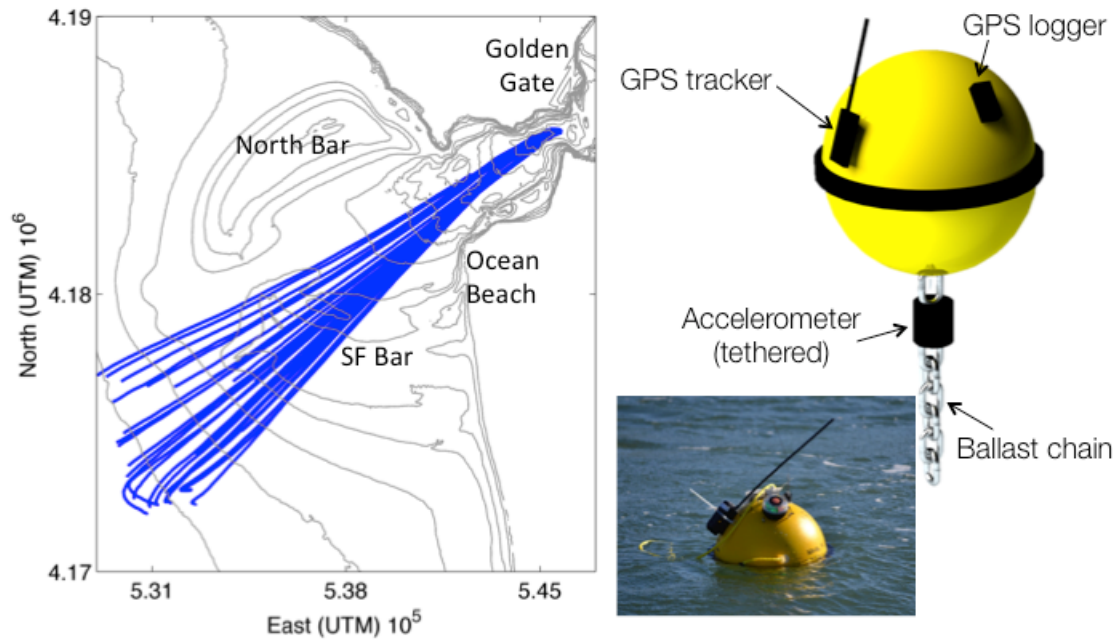
Figure 1.   Field site and instrumentation. The field site is in the San Francisco
            Bight where 30 drifters' tracks from the deployment on April 27, 2012,
            are shown in blue. A rendering of the WRD and a photo of the WRD
            floating in Monterey Bay are shown.
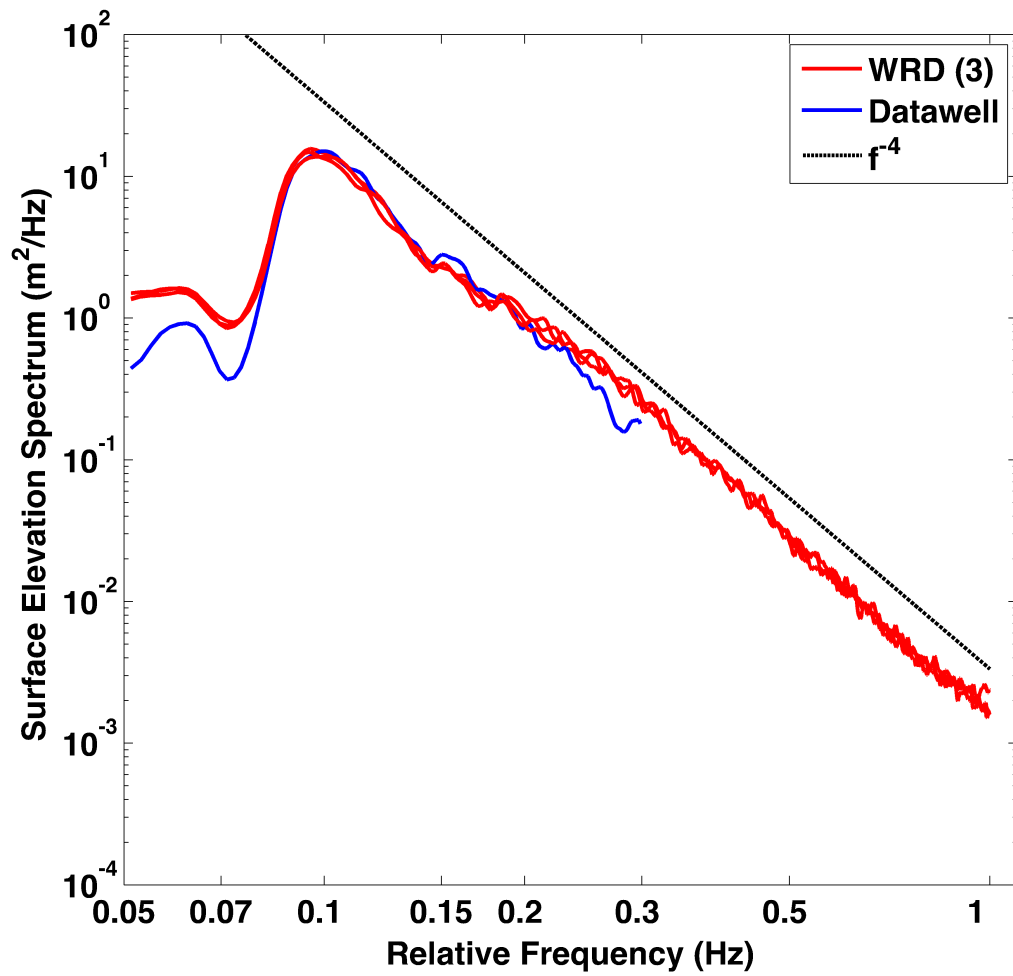
Figure 2.   Surface height spectral estimates from measurements made in the Monterey Bay by a Datawell Buoy (blue) and three collocated WRD buoys (red). Also shown is the f^{-4} spectral roll off (black dashed).
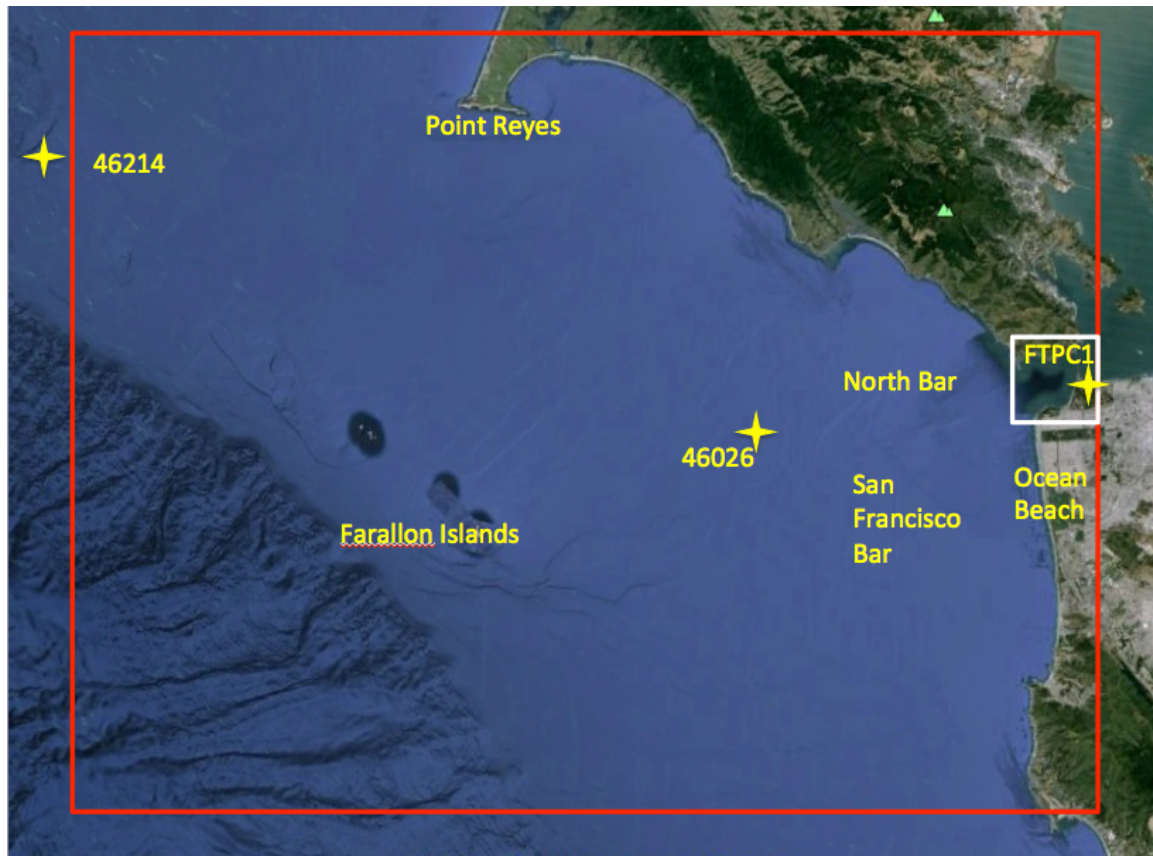
Figure 3.   Google earth image of the SWAN domain. The Point Reyes Buoy #46214 was used for spectral boundary conditions. The San Francisco Buoy #46026 provided wind forcing for the domain outside of the inlet. The red box outlines the SWAN domain. The small white box indicates the region of decreased wind forcing (based on wind and water-level station FTPC1).
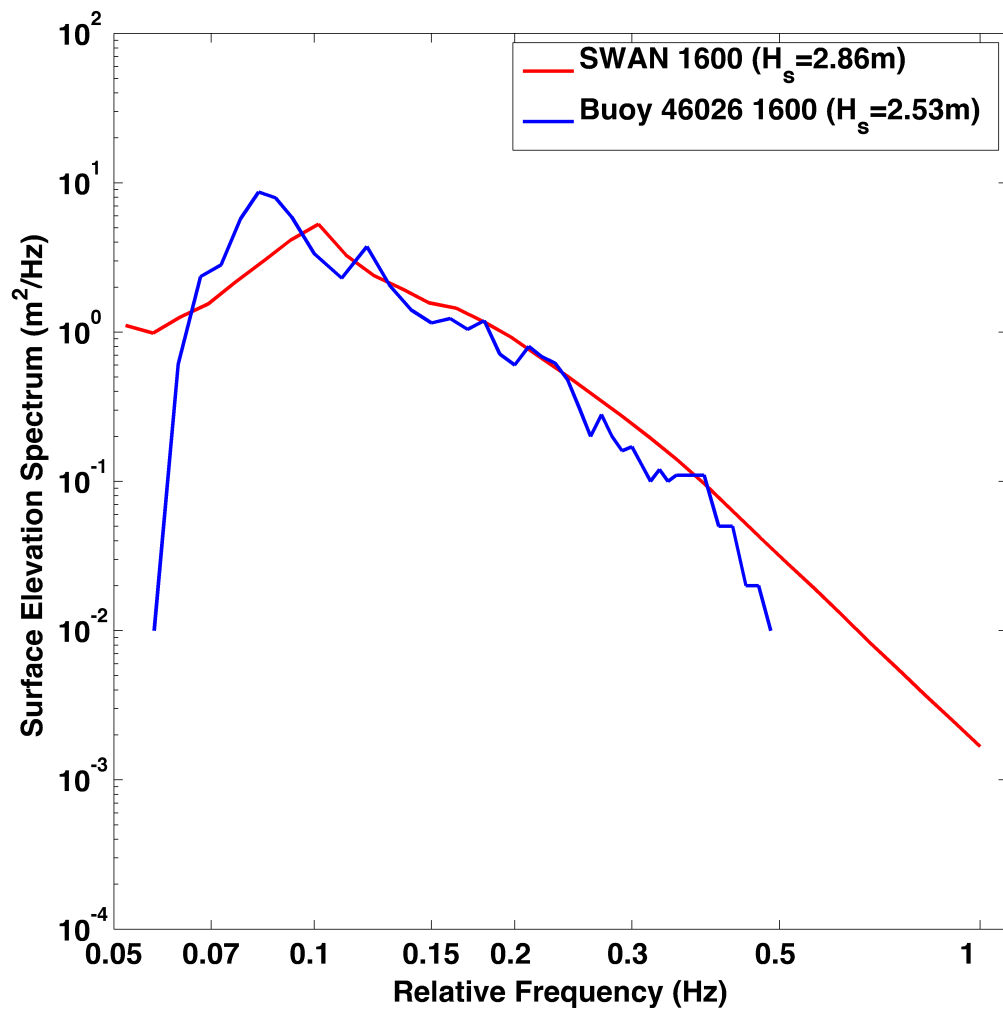
Figure 4.   Comparison of SWAN spectrum (red) with the San Francisco Buoy spectrum (blue) at 1500 UTC.
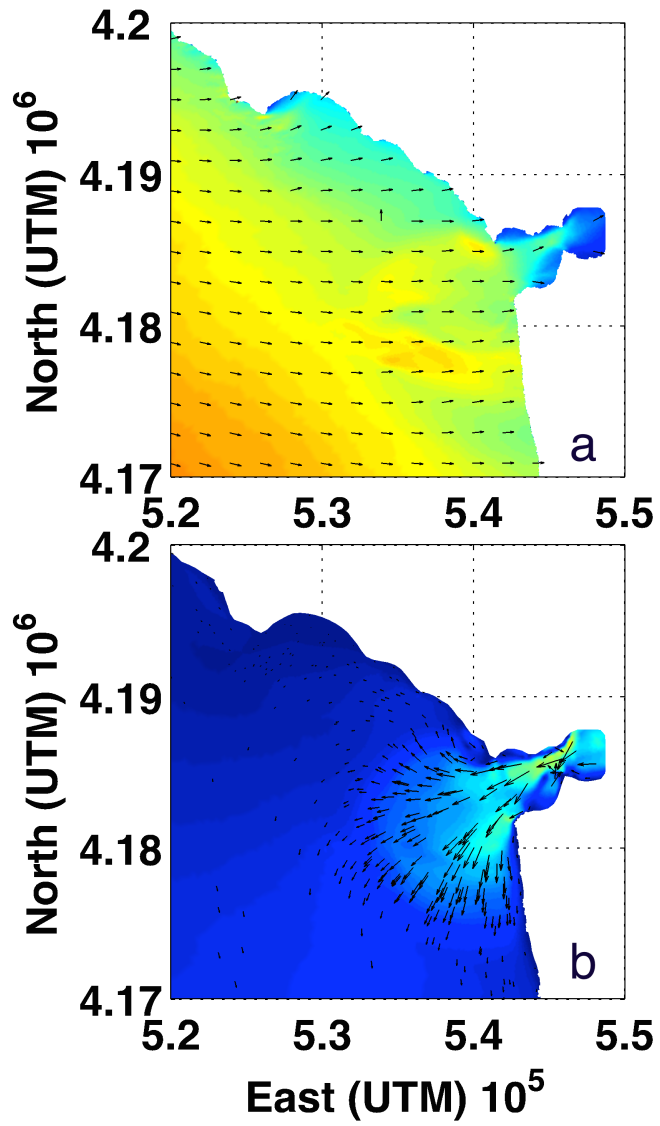
Figure 5.   SWAN significant wave height and mean wave direction (a), and the
Delft3D depth averaged velocity (b) at 1515 UTC.
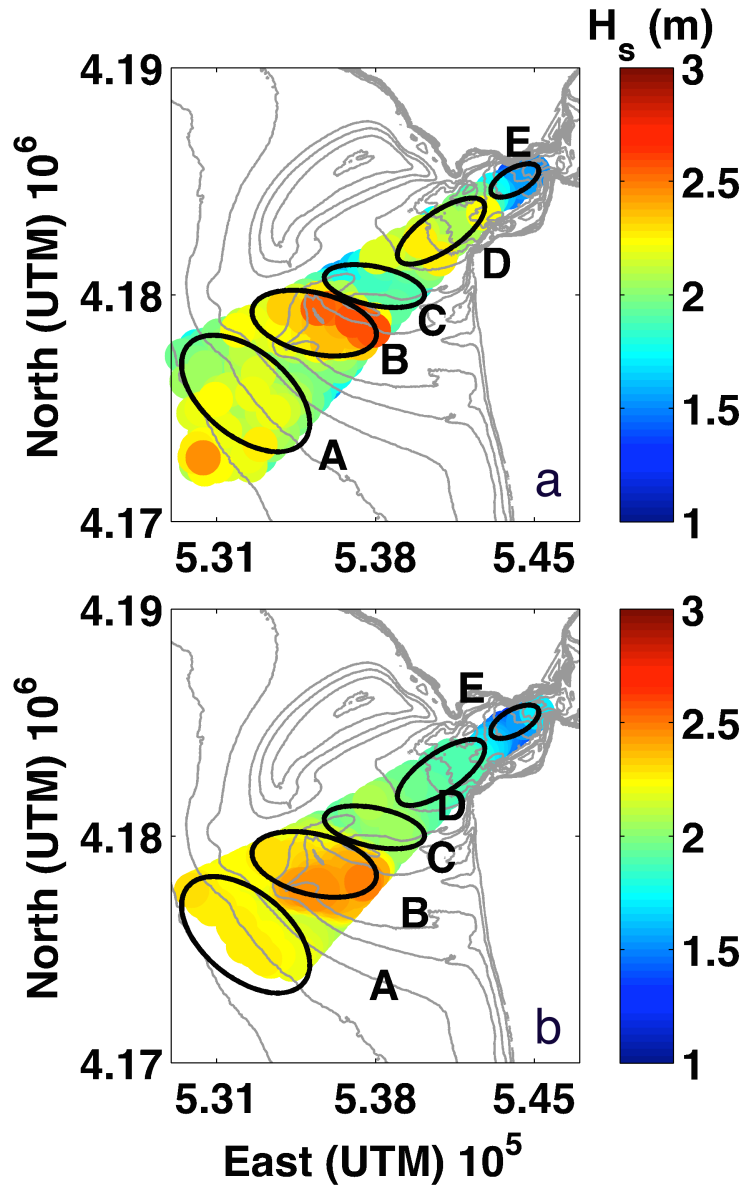
Figure 6. Spatial variability of significant wave height from the April 27, 2012 ebb deployment. Drifter observations (a) are compared with SWAN Sim#1 (b) significant wave heights that are evaluated at locations spatially and temporally consistent with the WRD. The WRD significant wave heights were estimated using the merged (GPS and Accelerometer) spectra. The estimates were obtained from 6.83 min records along each drift track and averaged spatially over a 500m x 500 m grid. The regions A-E indicate similar wave characteristics used for ensemble averaging regional spectral estimates in Figure 8a.
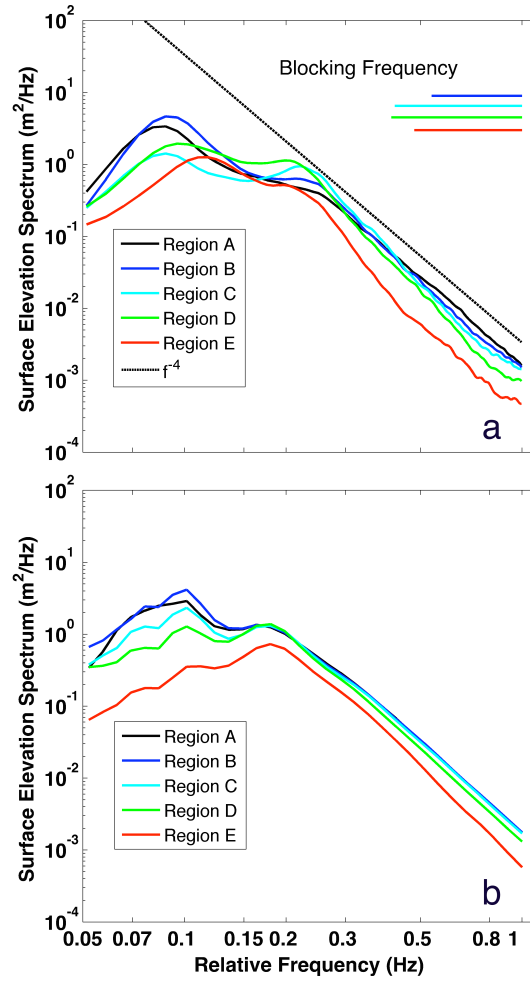
Figure 7. April 27, 2012 Ensemble averaged surface height spectra in regions A-E (A=offshore, B=over the SF Bar, C=east of SF Bar, D=approaches to SF Inlet, E=inlet, See Figure 6). Observed spectra (top) are compared with SWAN Sim #1 spectra calculated at the mean time of the drifter ensemble (bottom). Also indicated (top) are the f^{-4} spectral roll off (black dashed) and the blocking frequency in regions B-E.
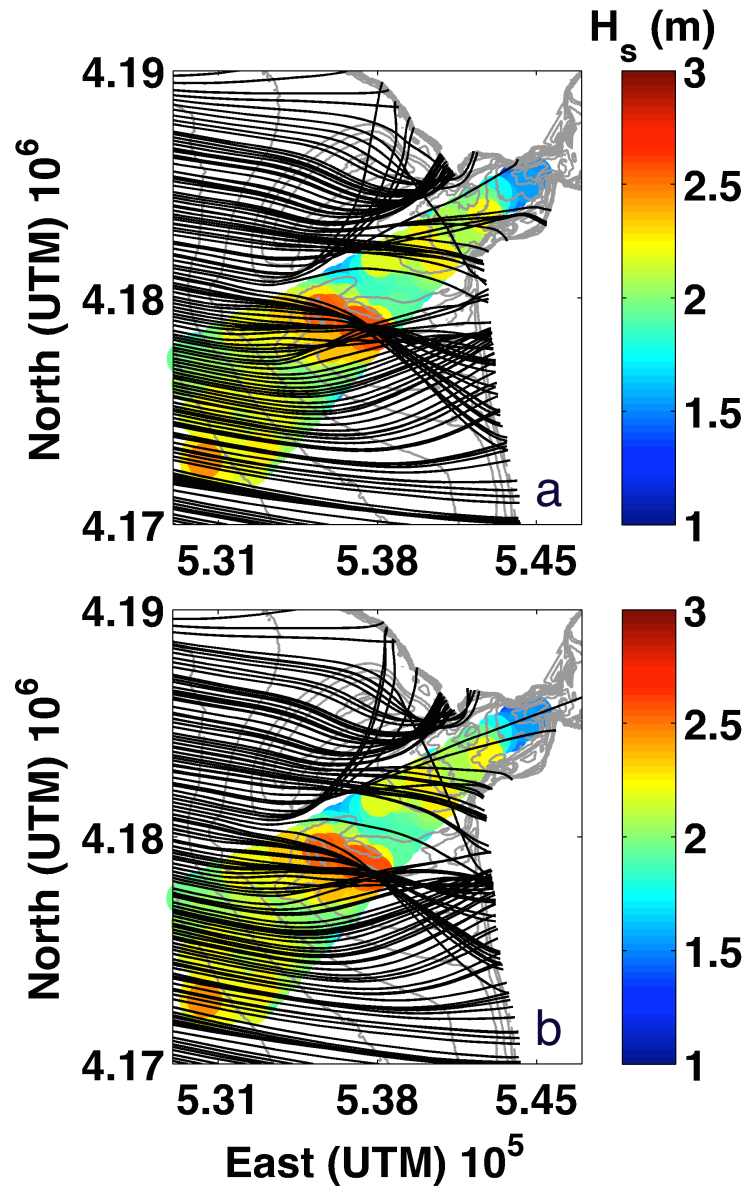
Figure 8.   WRD significant wave height estimates (color) with ray-trajectories
of 11 second swell (black lines) on bathymetry (grey curves). Rays
were calculated with wave current interaction using depth-averaged
currents from Delft3D (a), and with no currents (b).
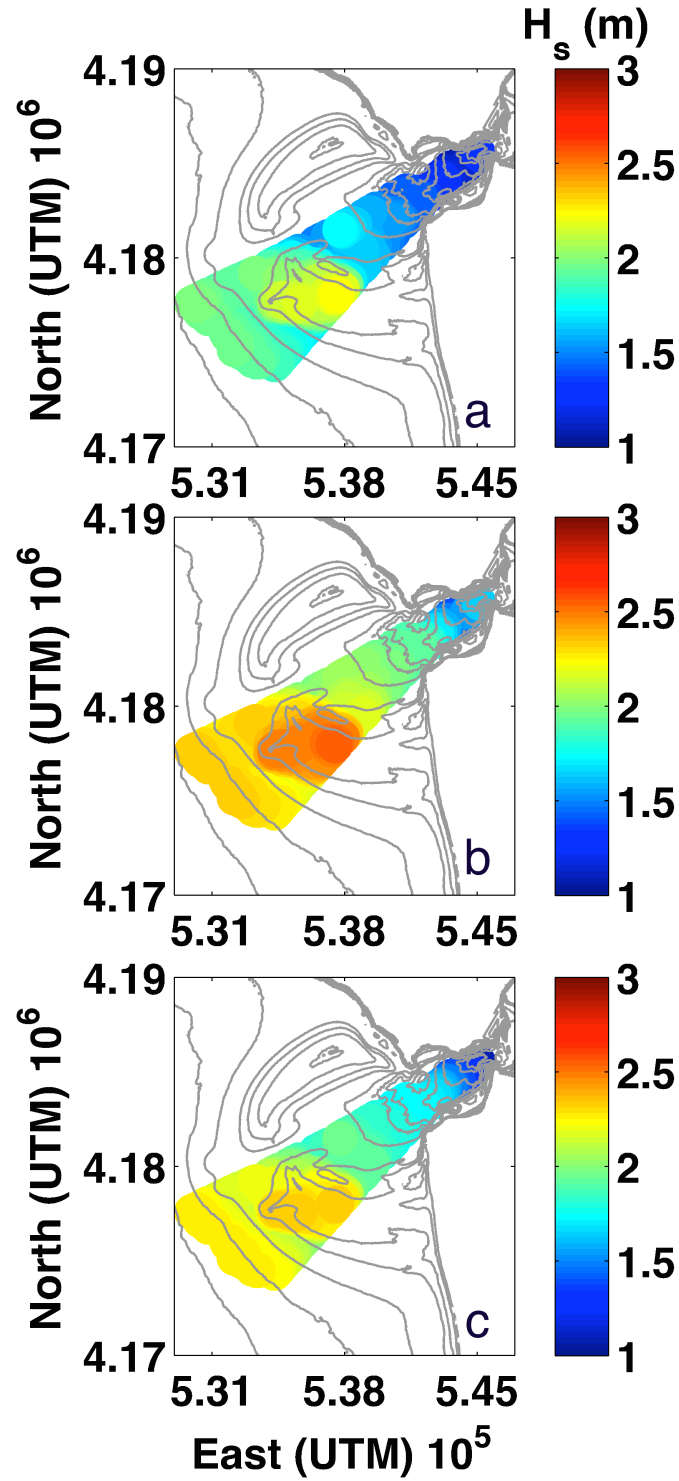
Figure 9.   Significant wave heights predicted in SWAN Sim #2 in which wind
is disabled (a), SWAN Sim#3 with bottom friction disabled (b), and
SWAN Sim #4 with currents disabled (c).
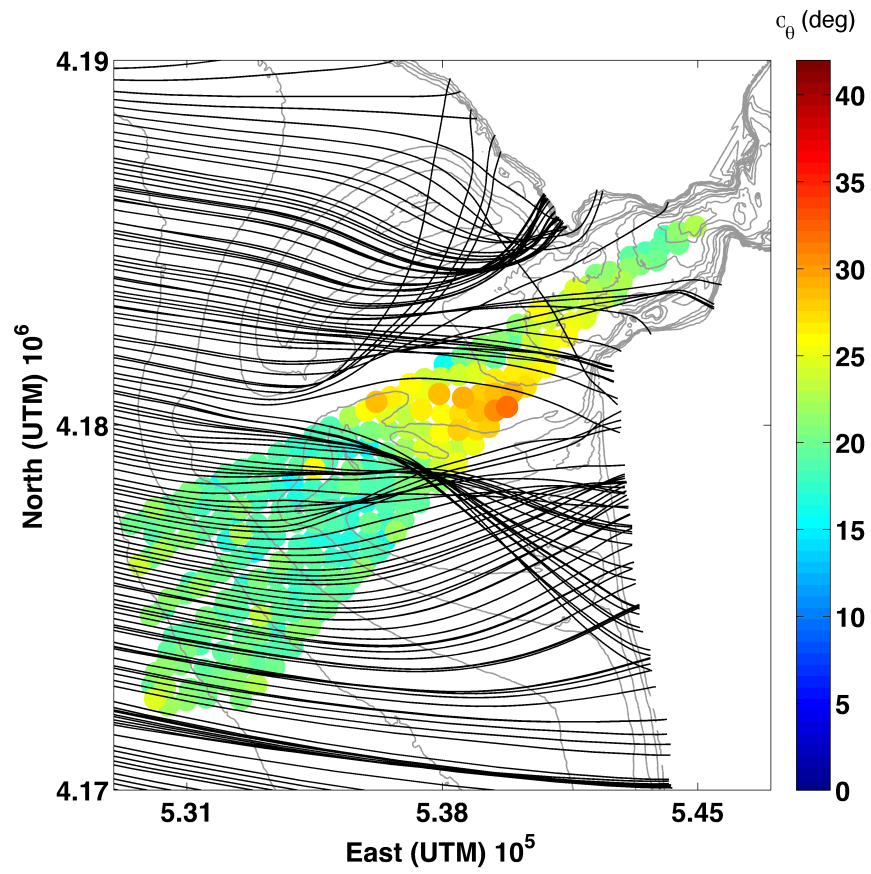
Figure 10.   Ray trajectories of 11 second swell (accounting for depth and current refraction) superposed on WRD estimates of bulk directional spread (second-order estimates, Appendix B).
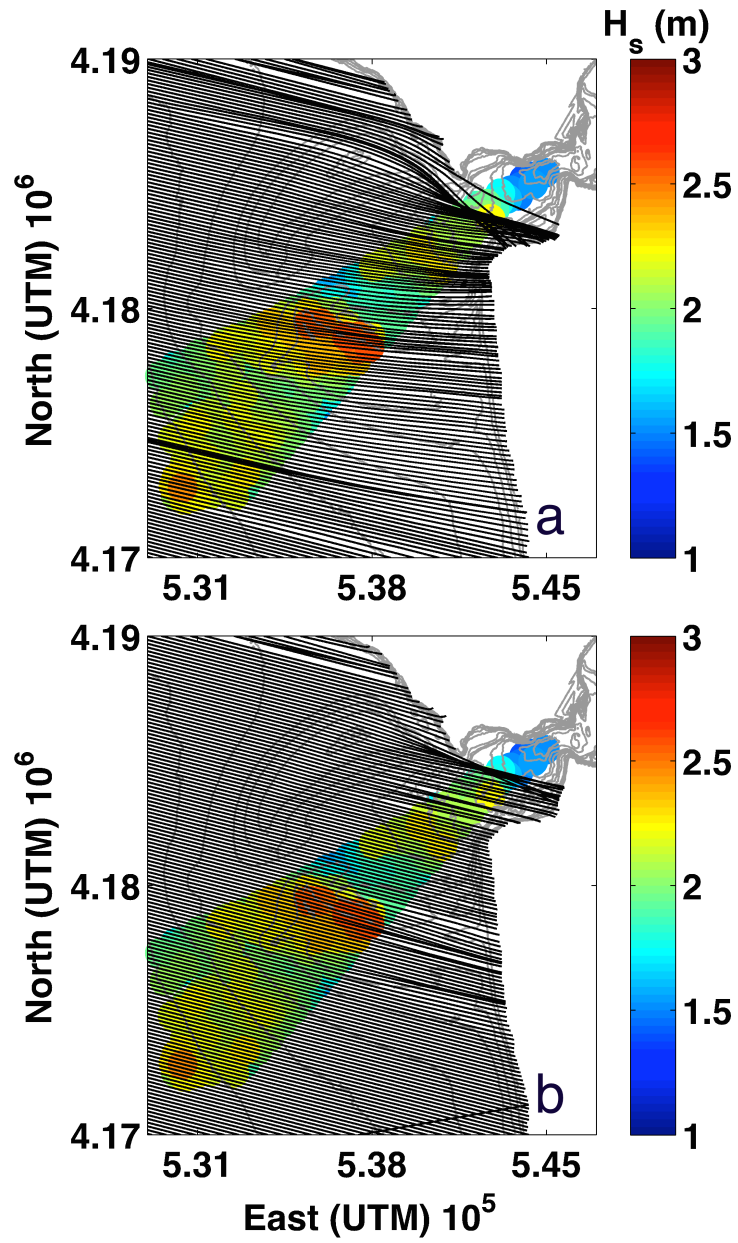
Figure 11.   WRD significant wave height estimates (color) with ray-trajectories of 5 second wind wave (black lines) on bathymetry (grey curves). Rays were calculated with wave current interaction using depth-averaged currents from Delft3D (top), and with no currents (bottom).
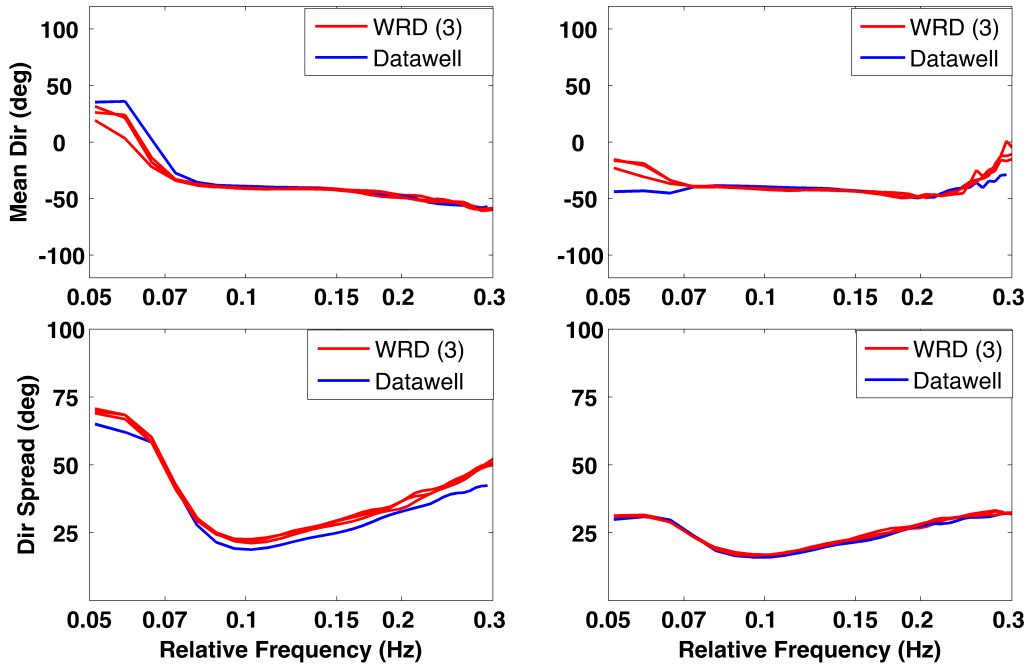
Figure 12.   Directional spectral estimates from the Datawell buoy (blue) and the WRD (red) deployed alongside the Datawell buoy during the Monterey Bay experiment. From top to bottom: mean direction and directional spread (as functions of frequency), respectively. The left panels show "traditional" estimates based on measurements of both vertical and horizontal surface motions. The right panels show alternative estimates based solely on horizontal surface motions.
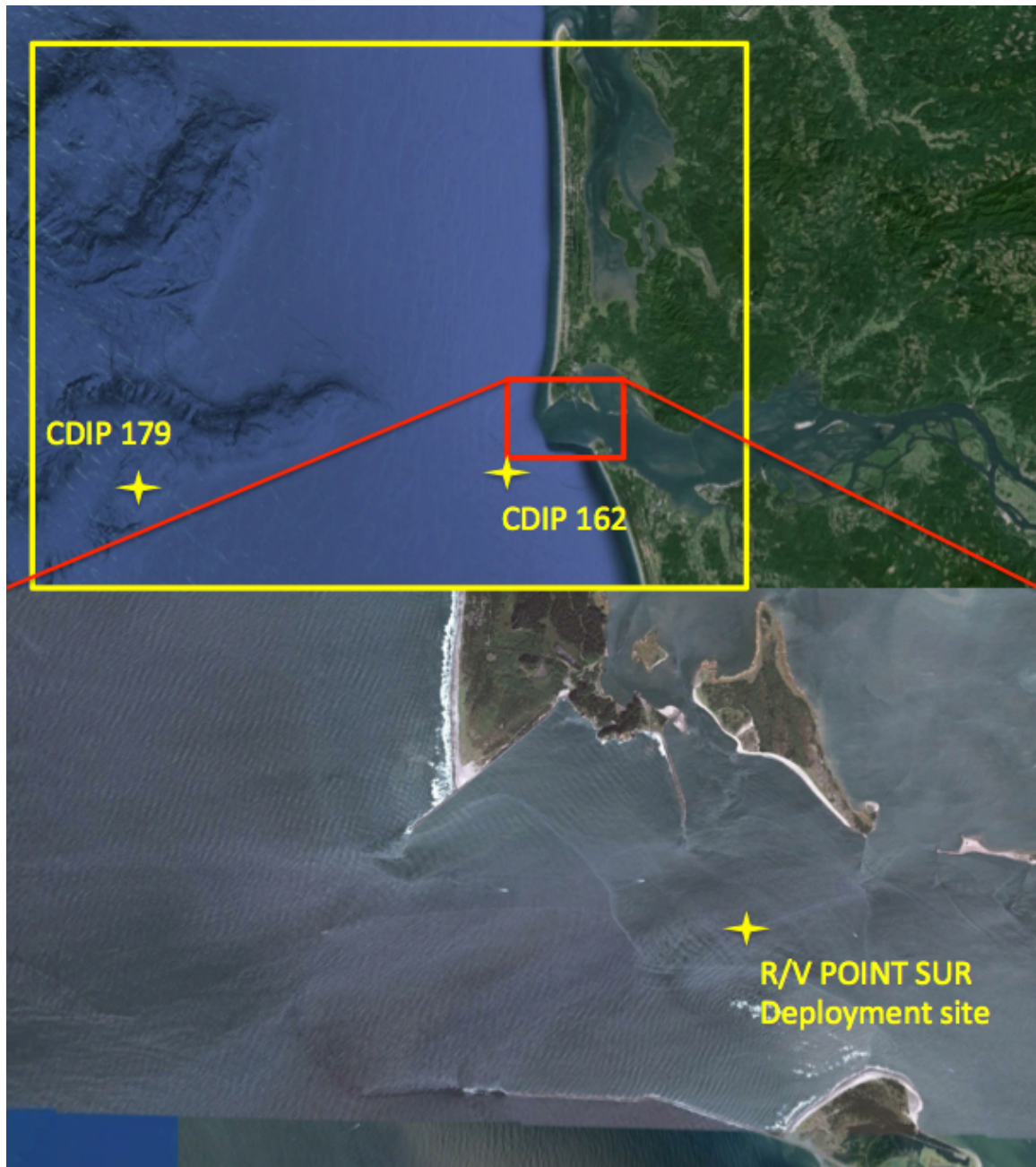
Figure 13. Google Earth image of the Mouth of the Columbia River and offshore approaches. The yellow box indicates the SWAN domain and the red box outlines the jetties at the entrance to the Columbia River.
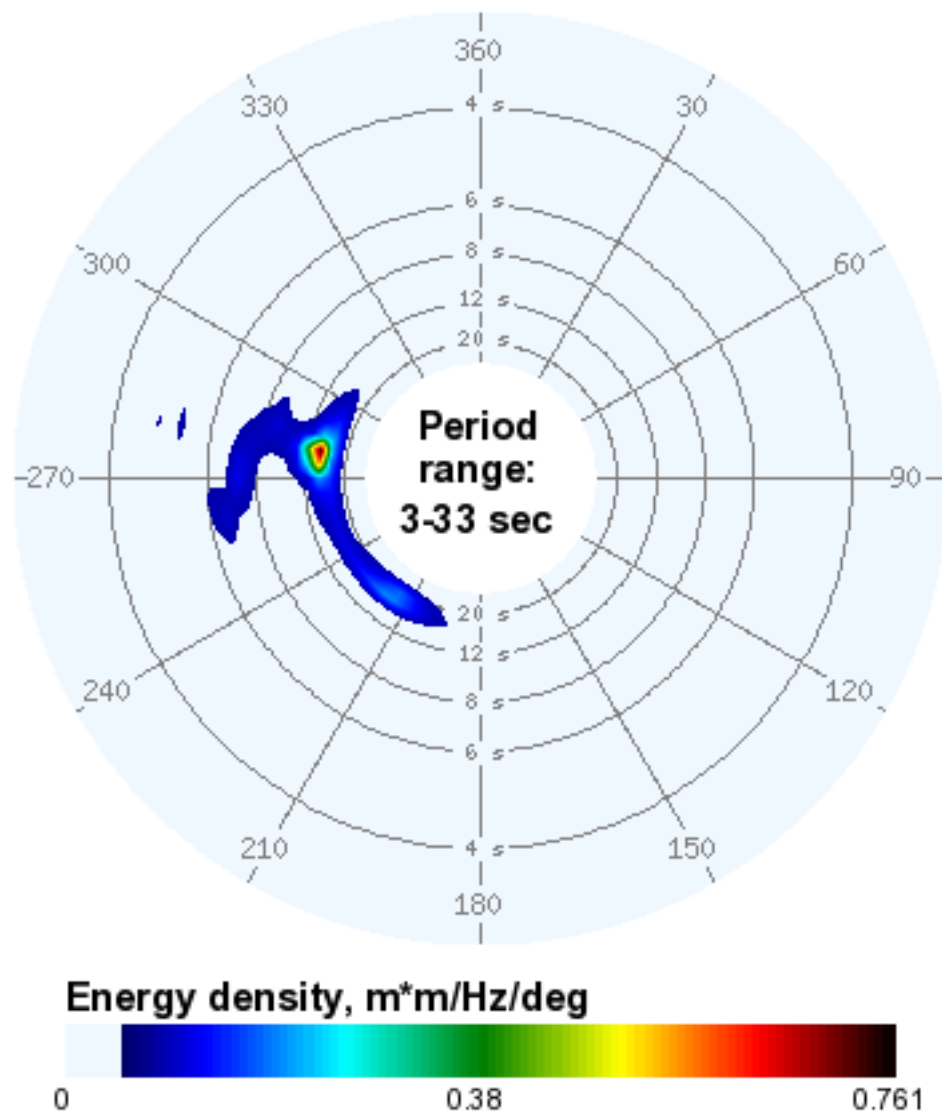
Figure 14.   Polar spectral density plot from CDIP station 179 in Astoria Canyon.
This location is representative of the wave conditions offshore of the
Mouth of the Columbia River. http://cdip.ucsd.edu

Figure 15.   Three different types of Wave Resolving Drifters (WRD). The WRD-A deployed from the R/V QUESTUARY (top left). The mix of WRD A-B-J on the deck of the R/V POINT SUR (top center). The WRD boat hook recovery (top right). The more advanced WRD-J (bottom).
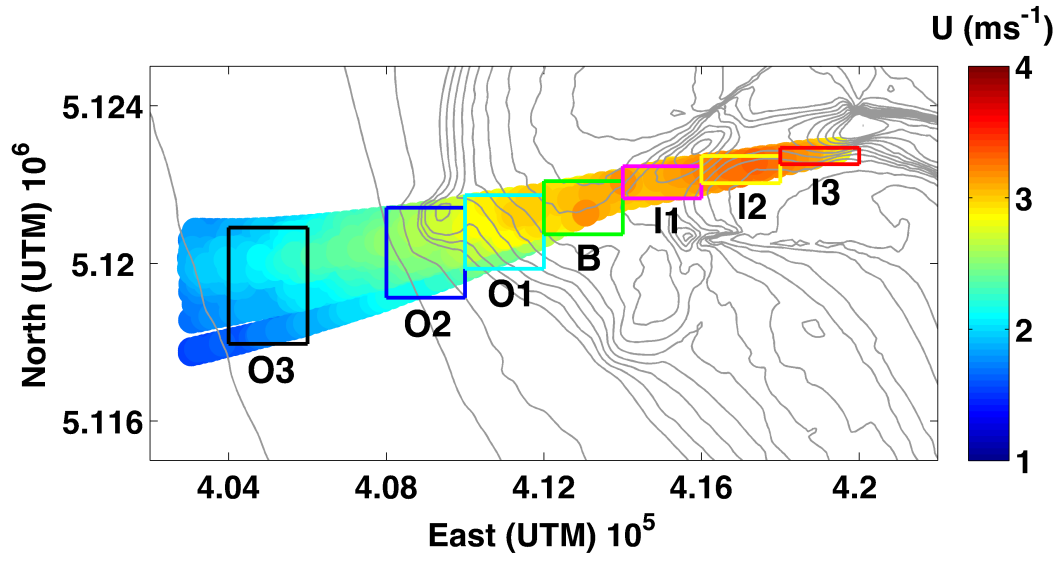
Figure 16.   Drift velocity measurements along drift tracks averaged temporally over 204.8 seconds and spatially onto a 100m x 100m grid. The measurements are plotted on the centroid of the data within each grid cell. The color bar on the right indicates the current scale. The rectangular boxes indicate regions where wave spectra were evaluated.
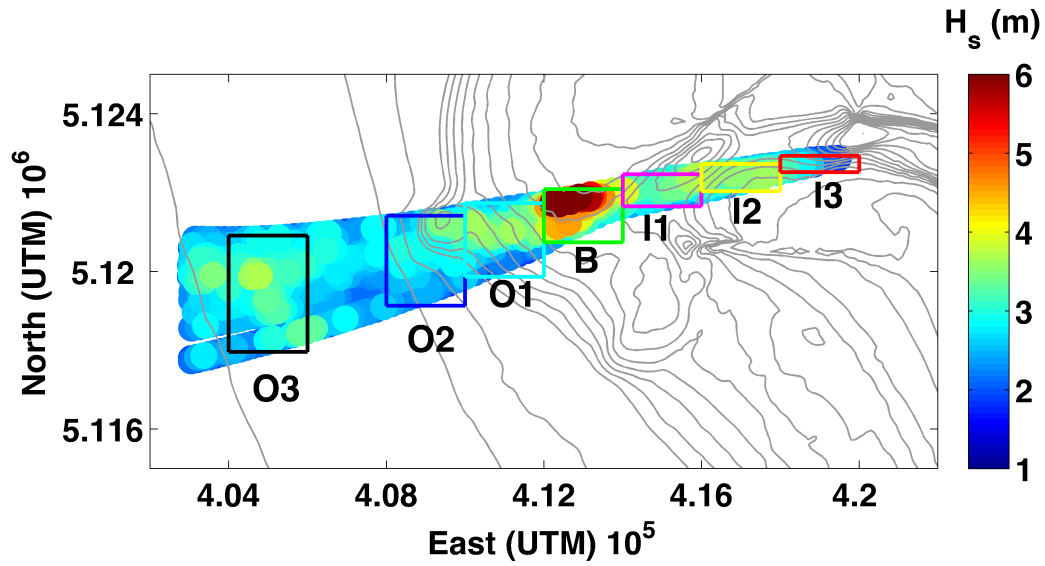
Figure 17. Spatial variability of significant wave height from the June 8, 2013 ebb deployment. The WRD observed significant wave heights were estimated using the combined GPS-Accelerometer spectra. The estimates were obtained from 3.4 min records along each drift track and averaged spatially over a 100m x 50 m grid. The colored zones coincide with the regional spectral estimates in Figure 19.
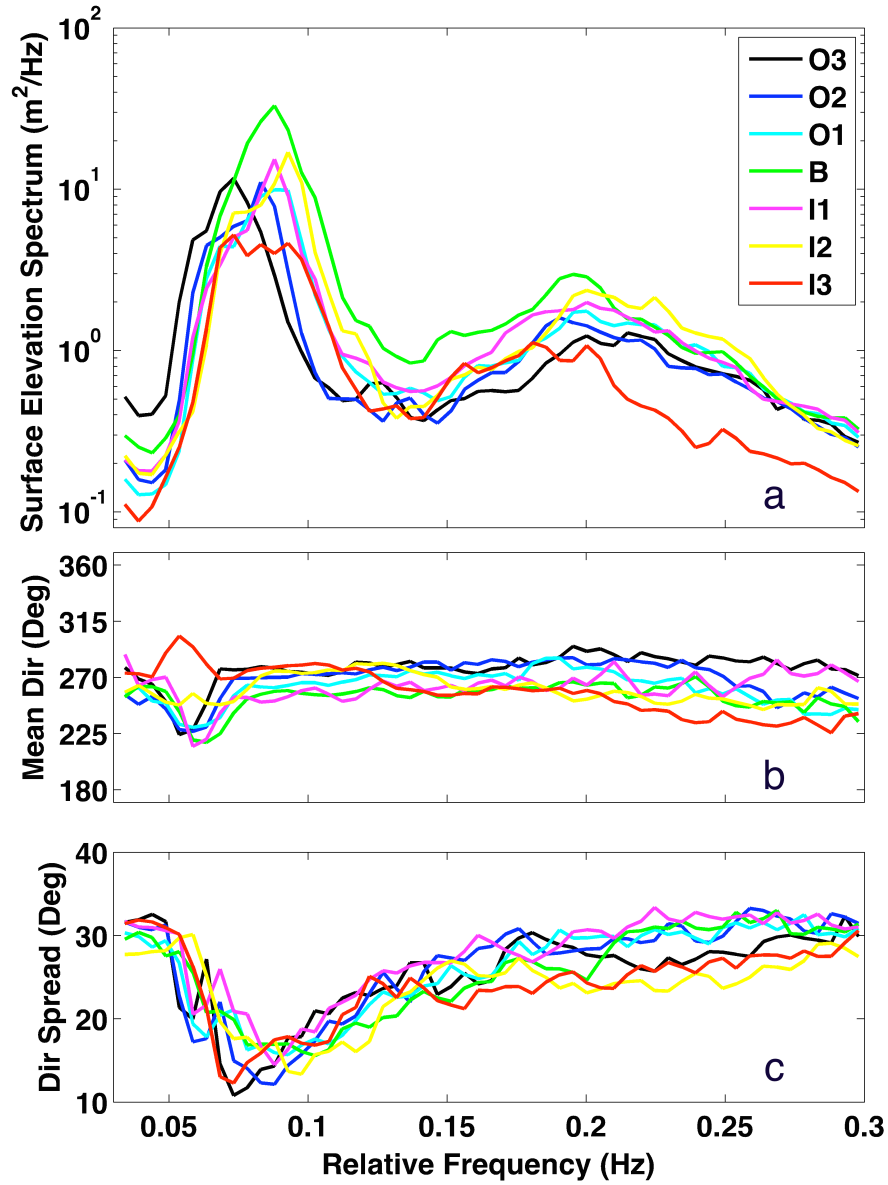
Figure 18.   June 08, 2013 Ensemble averaged surface height spectra in Zones O3-I3 (O3=offshore, O2=over the mound, O1=east of mound, B=over the Bar, I1=inside the Bar, I2=in the inlet, I3=in the river.) Surface elevation spectrum (a), mean direction (b), and directional spread (c). The directional estimates are based on 2nd order moments (Appendix B).
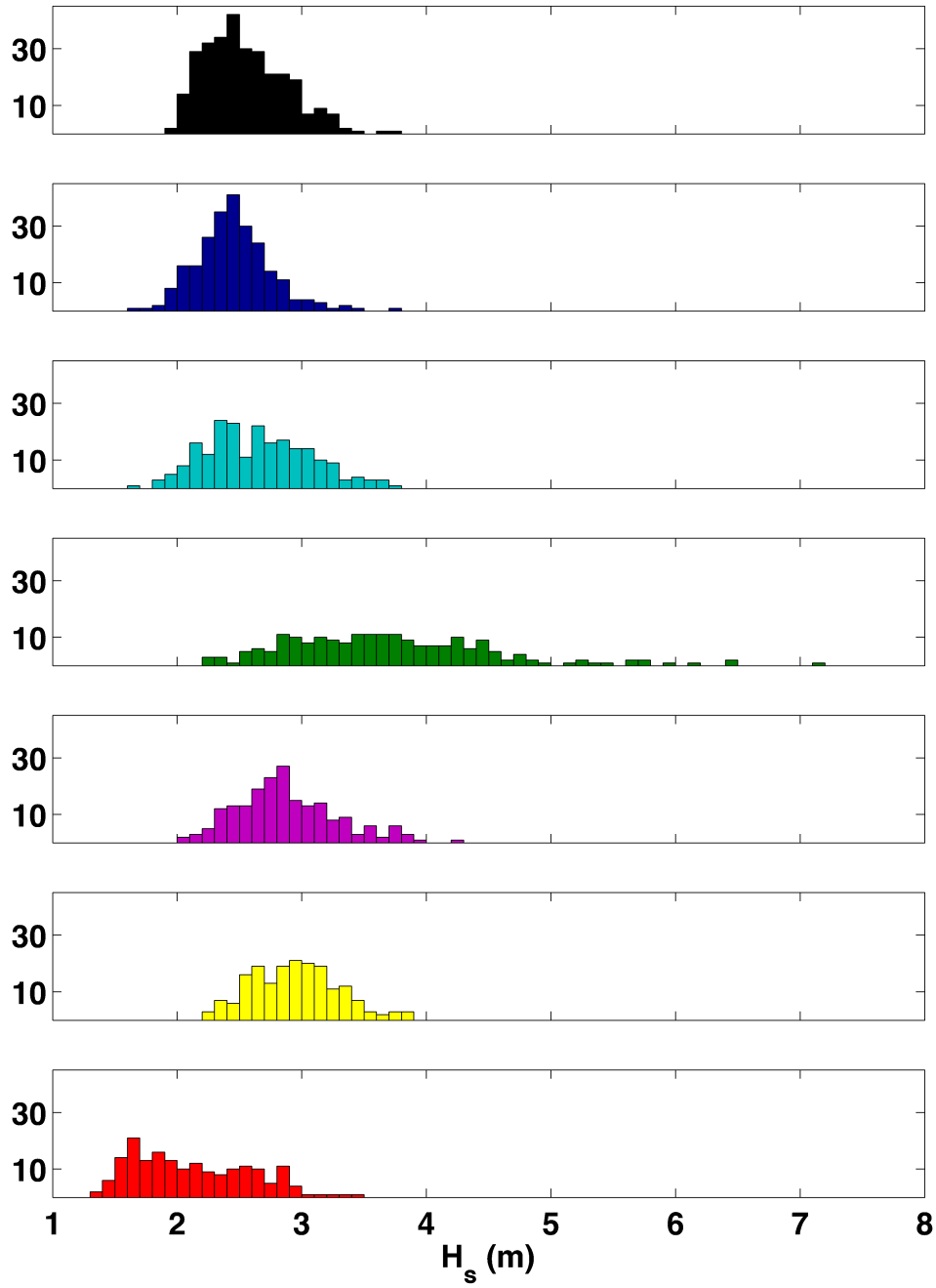
Figure 19.   Regional histograms of the individual WRD significant wave height
estimates within each zone. The zones are color coded to match the
spatial regions and spectra in Figure 18.
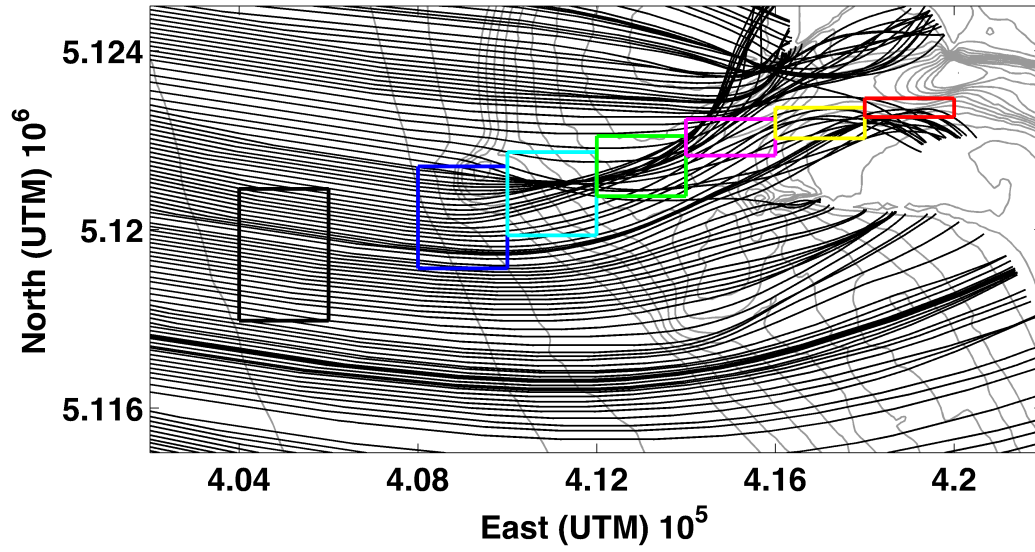
Figure 20.   Zones of interest (color) with ray-trajectories of 14-second swell waves from an offshore angle of 280 degrees (black lines) on bathymetry (grey curves). Rays were calculated with wave current interaction using depth-averaged currents from SELFE.
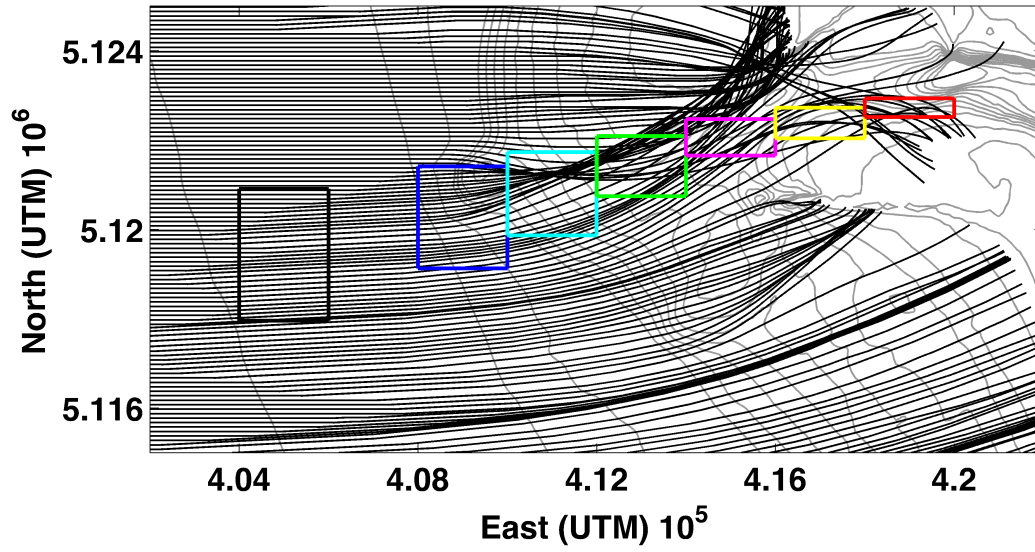
Figure 21.   Zones of interest (color) with ray-trajectories of 14-second swell
waves from an offshore angle of 270 degrees (black lines) on
bathymetry (grey curves). Rays were calculated with wave current
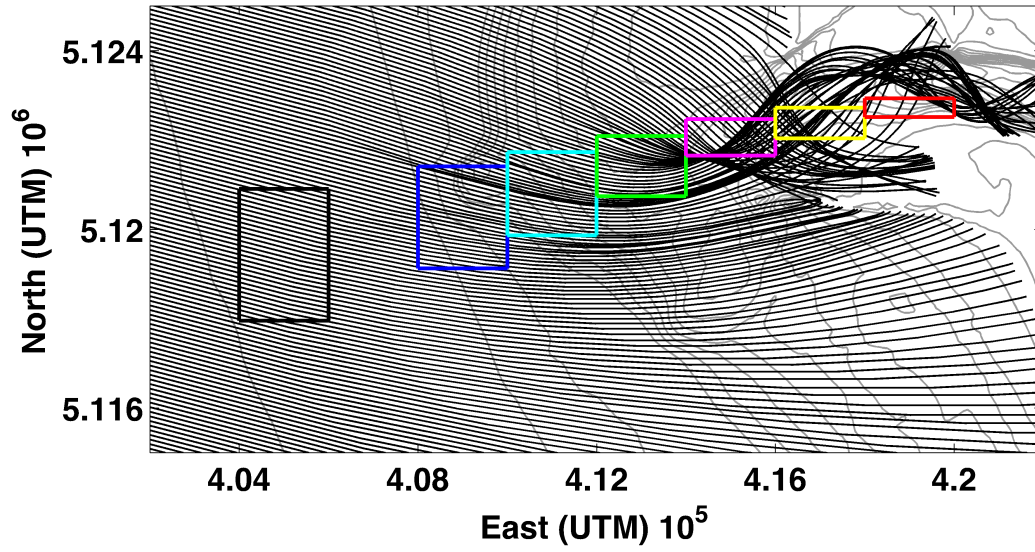interaction using depth-averaged currents from SELFE.

Figure 22.   Zones of interest (color) with ray-trajectories of 5-second wind waves from an offshore angle of 285 degrees (black lines) on bathymetry (grey curves). Rays were calculated with wave current interaction using depth-averaged currents from SELFE.
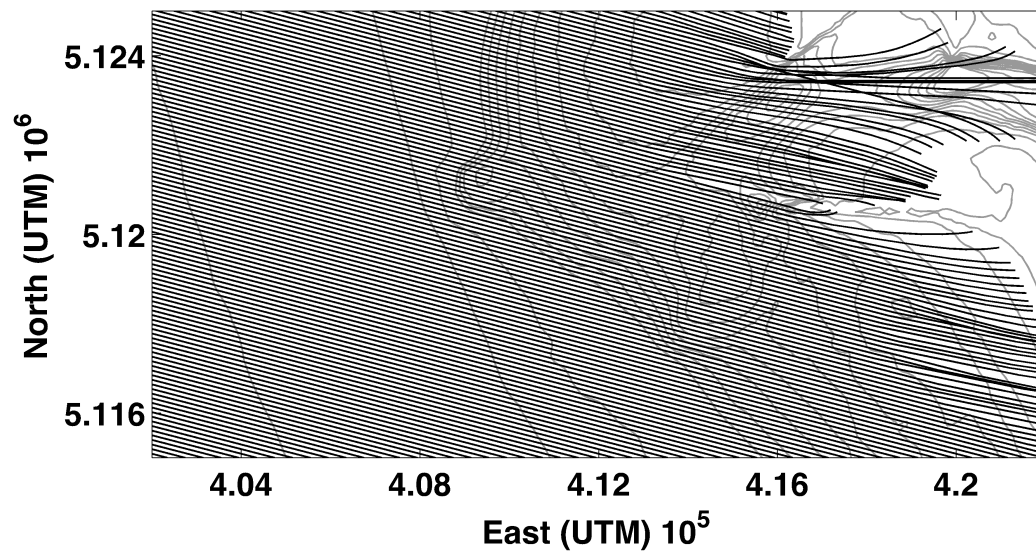
Figure 23.   Ray-trajectories of 5-second wind waves from an offshore angle of
285 degrees (black lines) on bathymetry (grey curves). Rays were
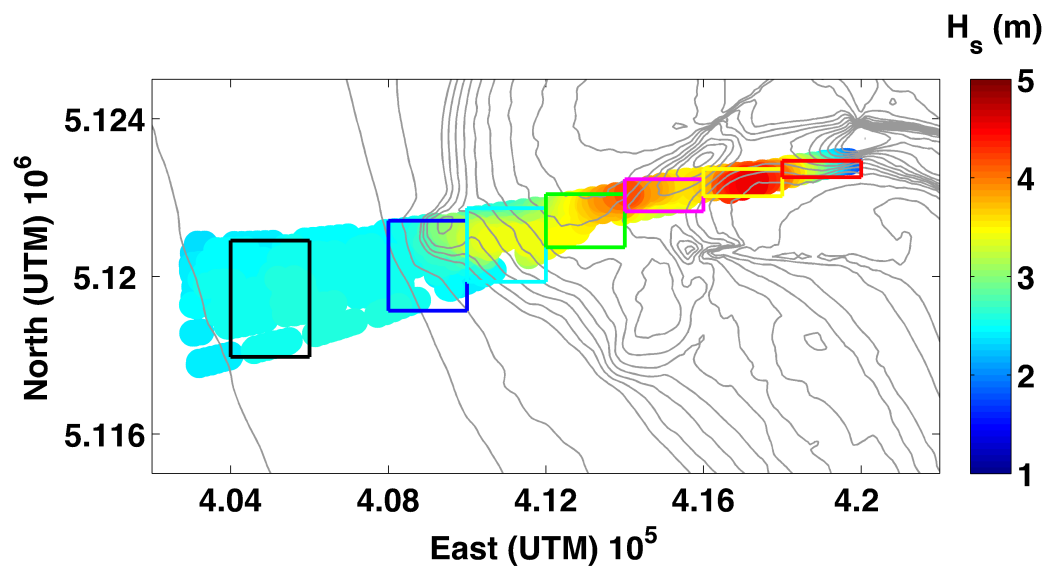calculated with wave current interaction disabled.

Figure 24.   SWAN Sim #1 significant wave height predictions. The Zones of interest coincide with those from the WRD discussion and the SWAN spectra in Figure 25.
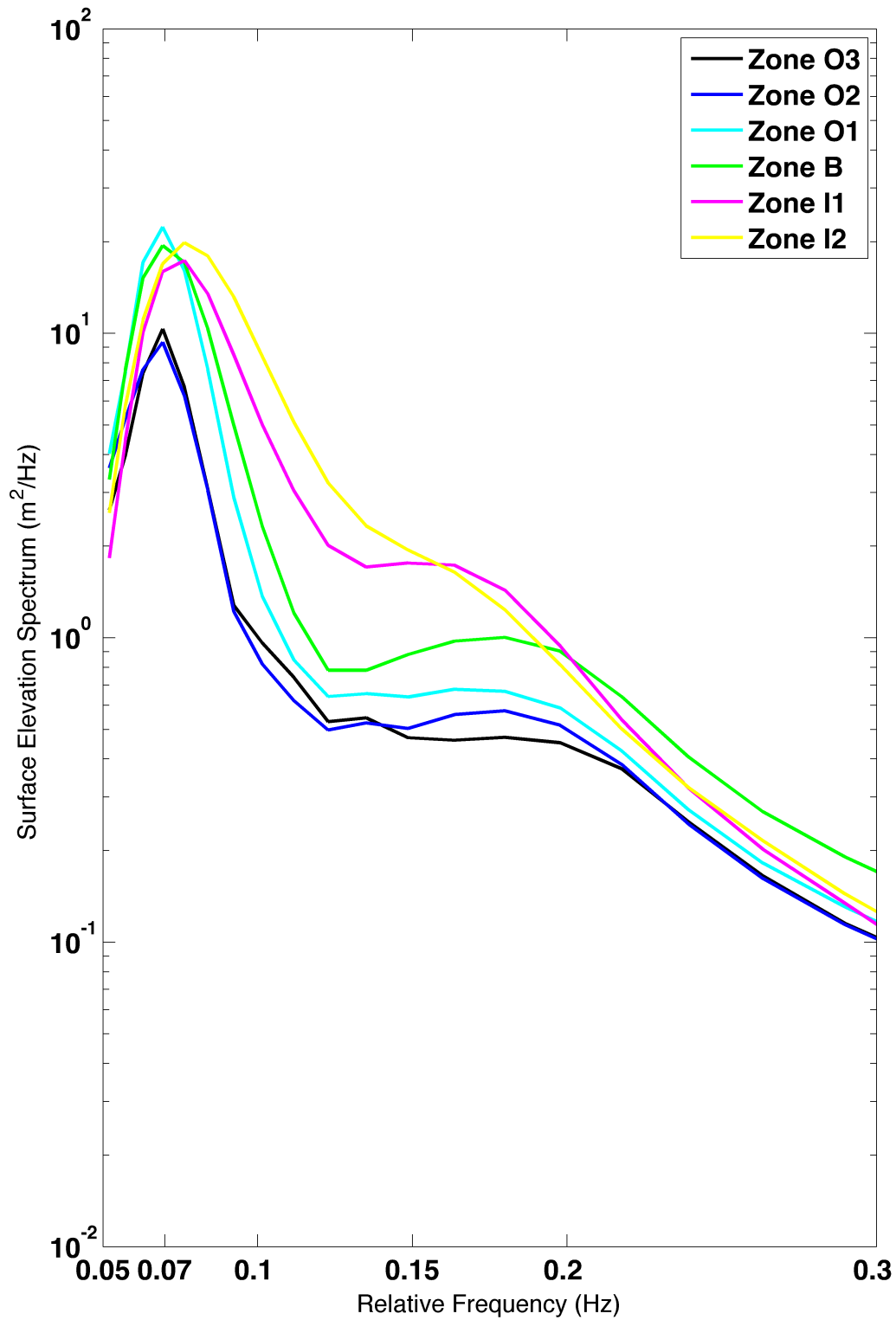
Figure 25.   SWAN spectra from Sim #1 are calculated at grid points near the center of the Zones.
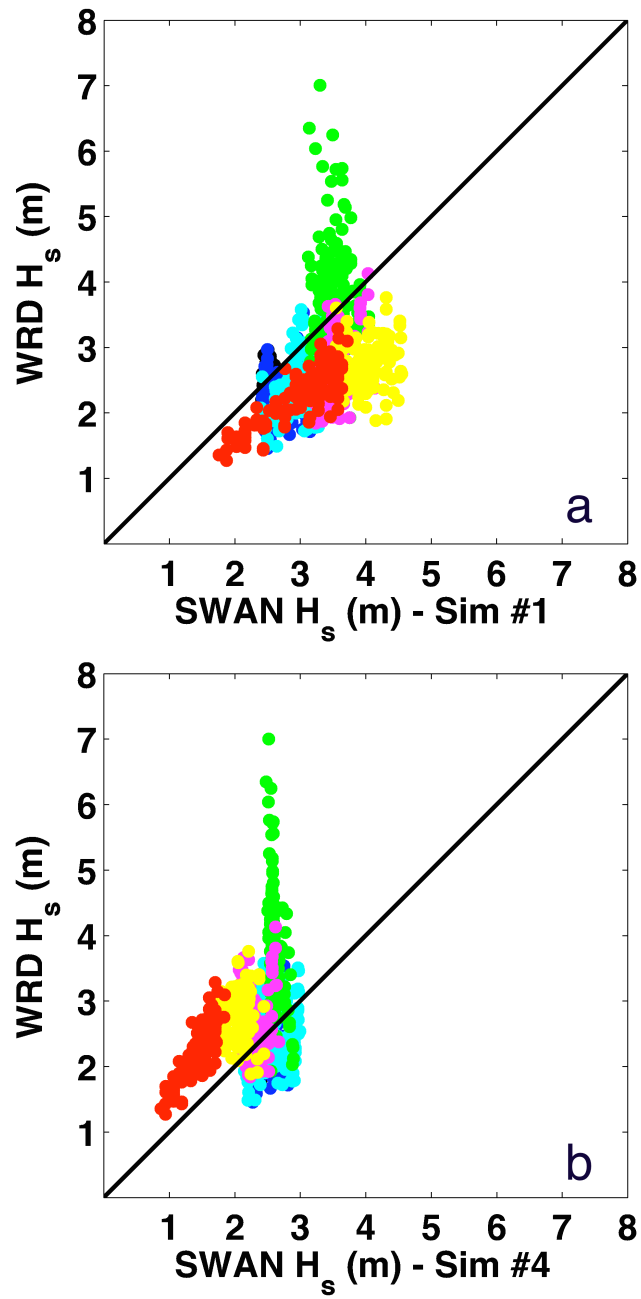
Figure 26.   Comparison of significant wave height estimates from the WRD estimates and SWAN Sim #1 (a) and Sim #4 (b) collocated in space and time. The colors are consistent with the Zones in Figures 24 and 25.
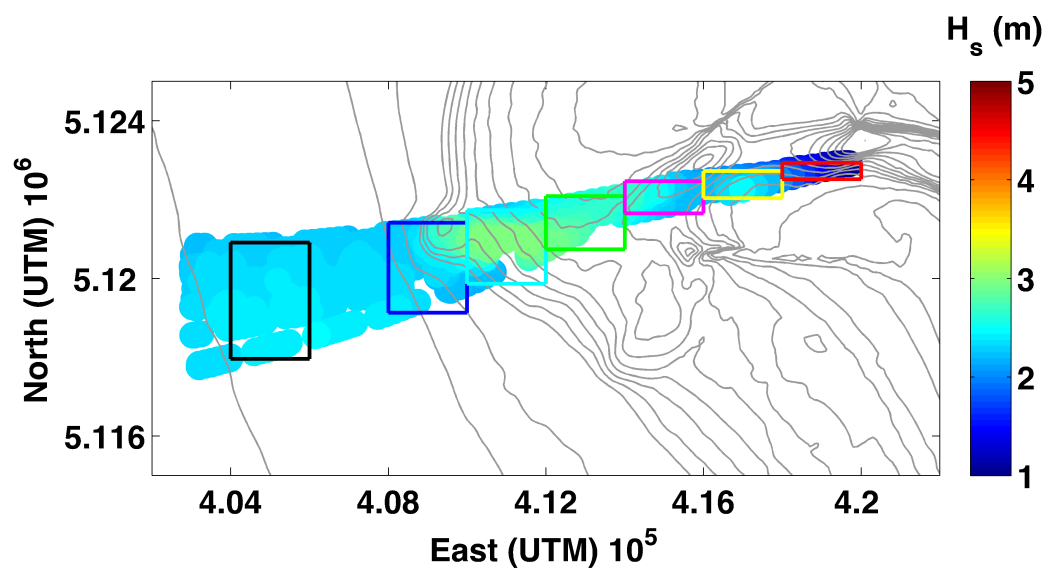
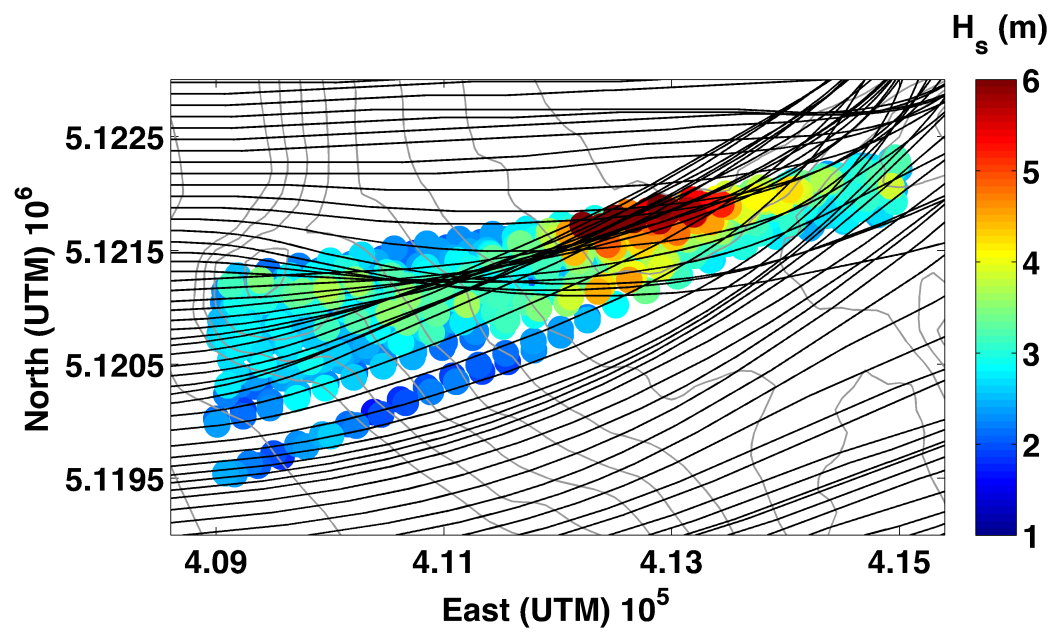Figure 27.   SWAN significant wave height with currents disabled.

Figure 28.   Significant wave height estimates from the WRD with rays from an offshore wave direction of 275 and a 14 second period.
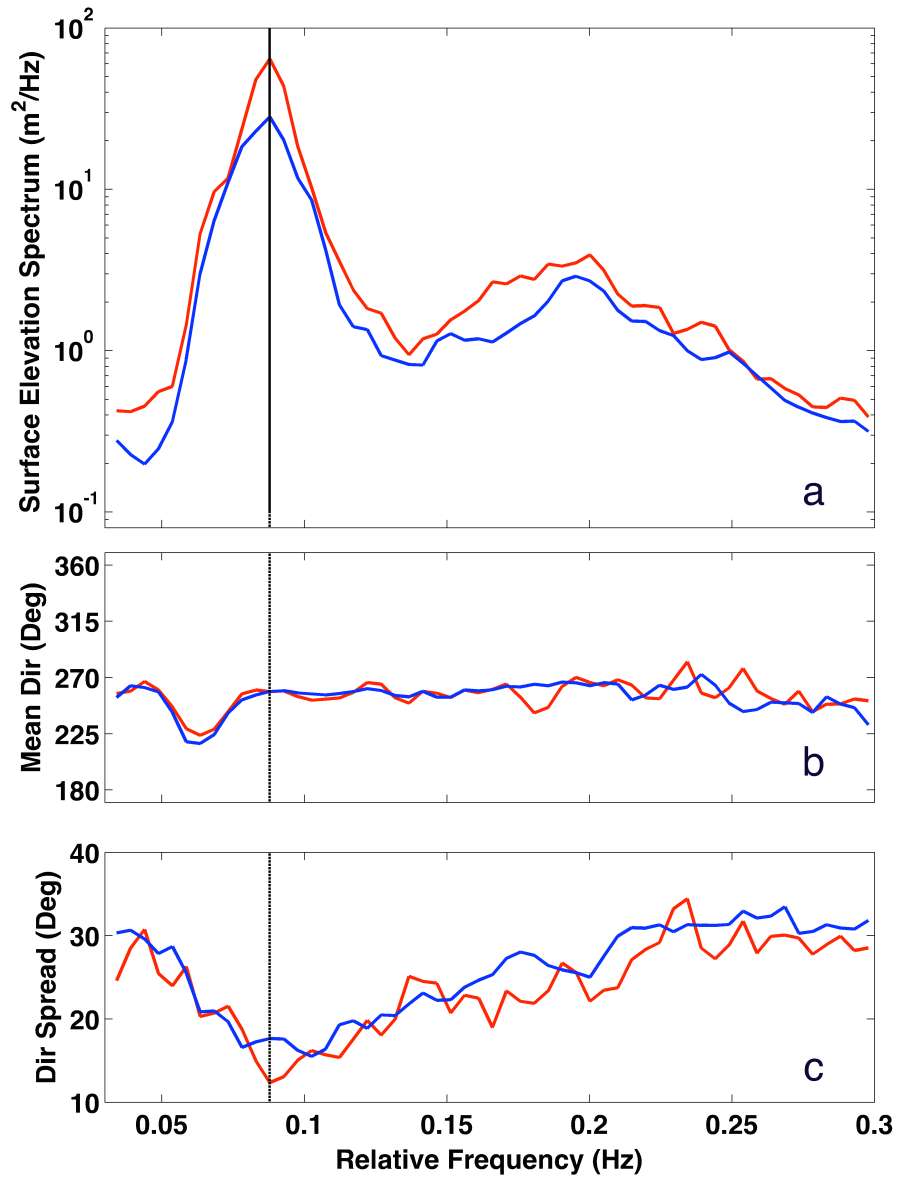
Figure 29.   Ensemble averaged surface height spectra in Zone B for enhanced
(red) and un-enhanced (blue) local wave conditions. Surface elevation
spectrum (a), mean direction (b), and directional spread (c).

Figure 30.   Significant wave height plotted against directional spread in Zone B.

Figure 31.   A time series of orbital velocities from one of the drifters passing over the Bar. The time series is shown in reverse to match the spatial variation in Figure 29 from 4.12 to 4.14 10^5 (UTM).

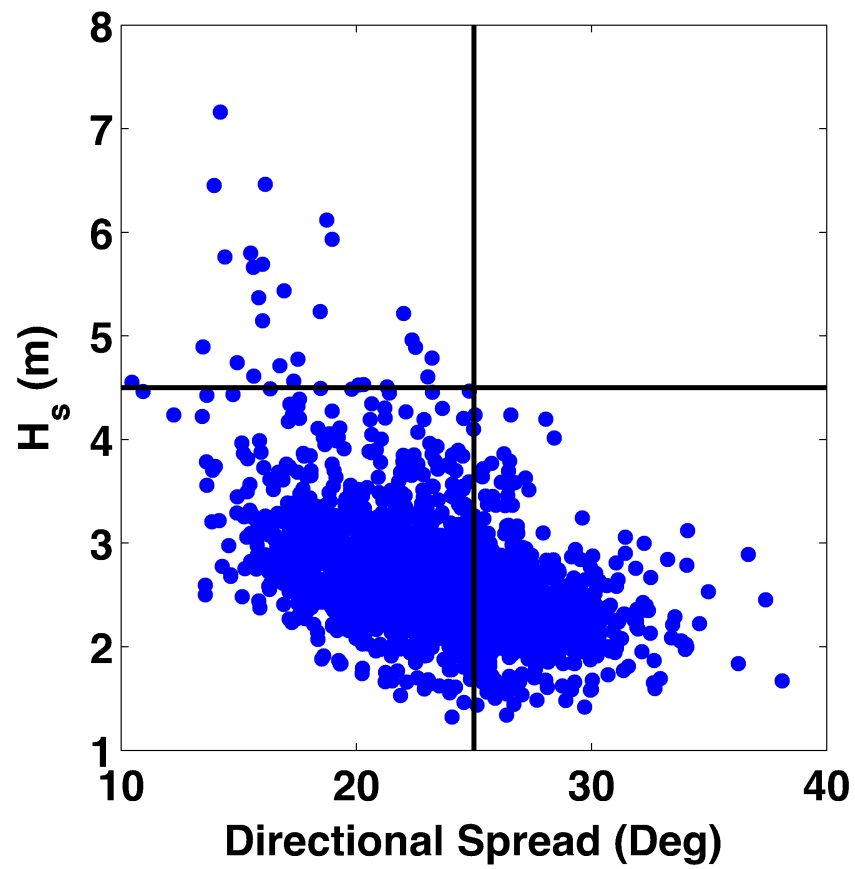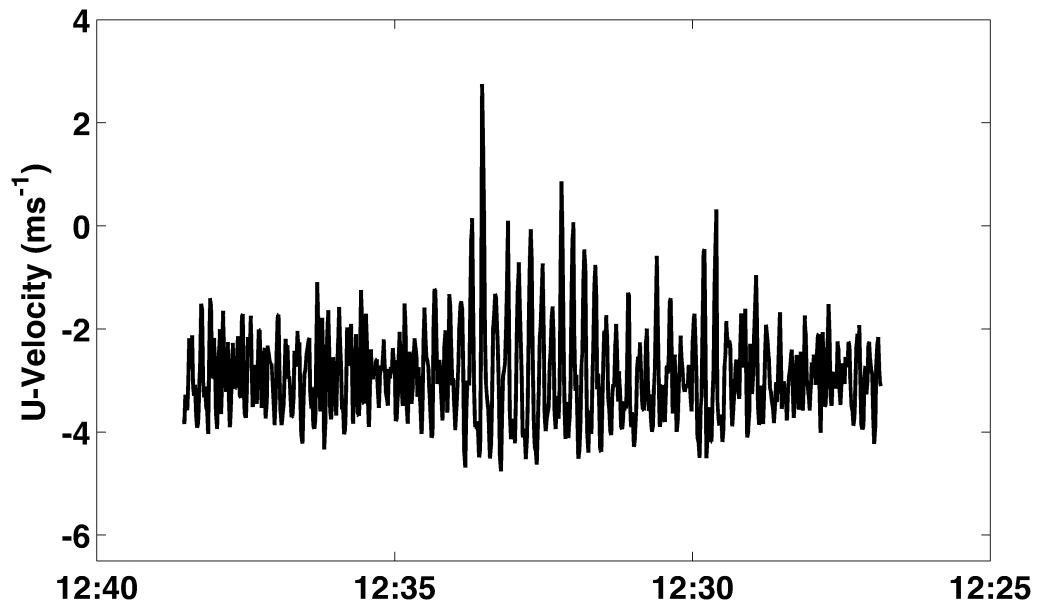THIS PAGE INTENTIONALLY LEFT BLANK

LIST OF REFERENCES

Anctil, F., M. A. Donelan, G. Z. Forristall, K. E. Steele, and Y. Ouellet, 1993: Deep-water field evaluation of the NDBC-SWADE 3-m discus directional buoy. *J. Atmos. Oceanic Technol*. **10**, 97–112.

Alves, J.H.G.M, and M. L. Banner, 2003: Performance of a saturation-based dissipation-rate source term in modeling the fetch-limited evolution of wind waves. *J.Phys. Oceanogr*. **33**, 1274–1298.

Banner, M. L., 2000: Breaking probability for dominant waves on the sea surface. *J.Phys.Oceanogr*., **30**, 3145–3160.

Barnard P. L., D. M. Hanes, D. M. Rubin, and R. G. Kvitek, 2006: Giant sand waves at the mouth of San Francisco Bay. *Eos Trans. AGU*, **87**(29), 285–289.

Barnard P.L., J. E. Hansen, and L. H. Erikson, 2012: Synthesis study of an erosion hot spot, Ocean Beach, California. *J. Coast. Res*. **28**(4), 903–922.

Bascheck B., D. M. Farmer, and C. Garrett, 2006: Tidal fronts and their role in air-sea gas exchange. *J. Mar. Res*., **64**, 483–515.

Battjes, J. A., and J. P. F. M. Janssen, 1978: Energy loss and set-up due to breaking of random waves. *Proc. 16th Int. Conf. Coastal Eng.,* Hamburg, 569–587.

Battjes, J. A., T. J. Zitman, and L. H. Holthuijsen, 1987: A reanalysis of the spectra observed in JONSWAP. *J. Phys. Oceanogr*. **17**, 1288–1295.

Booij, N. R., R. C. Ris, and L. H. Holthuijsen, 1999: A third-generation wave model for coastal regions, 1, Model description and validation. *J. Geophys. Res*., **86**, 10, 961–10,973.

Bretherton, F. P., C. J. T Garrett, 1968: Wavetrains in inhomogenous moving media. *Proceedings of the Royal Society of London. Series A, Mathematical and Physical Sciences*, **302**(1471) 529–554.

Cavaleri, L., and P. Malanotte-Rizzoli, 1981: Wind wave prediction in shallow water: Theory and applications. *J. Geophys. Res.,* **86**(11, 10) 961–973.

Cavaleri, L., 2009: Wave modeling—Missing the peaks. *J. Phys. Oceanogr.* **39**(11), 2757–2778.

Chawla A., and J. T. Kirby, 2002: Monochromatic and random wave breaking at blocking points. *J. Geophys. Res*., **107**(C7), 3067

Columbia River Bar Pilots, Cited 2014: Safety record. [Available online at
http://www.columbiariverbarpilots.com/columbiariverbarpilots_safety.html.]

Dodet, G., X. Bertin, N. Bruneau, A. B. Fortunato, A. Nahon, and A. Roland, 2013:
Wave-current interactions in a wave-dominated tidal inlet. *J. Geophys. Res.* **118**,
1587–1605.

de Vries, J. J., J. Waldron, and V. Cunningham, 2003: Field tests of the new Datawell
DWR-G GPS wave buoy. Sea Technol., **44**, 50–55. [Available online at
http://download.datawell.nl/documentation/datawell_publication_dwr-
g_seatechnologydec2003_2003-12-01.pdf.

Elias, E. P. L., G. Gelfenbaum, and A. J. Van der Westhuysen, 2012: Validation of a
coupled wave-flow model in a high-energy setting: The mouth of the Columbia
River. *J. Geophys. Res*., **117**, C09011, doi:10.1029/2012JC008105

Elias, E. P. L., and J. E. Hansen, 2012: Understanding processes controlling sediment
trans-ports at the mouth of a high-energetic inlet system (San Francisco Bay, CA).
Marine Geology, Special Issue San Francisco Bay.
http://dx.doi.org/10.1016/j.margeo.2012. 07.003

Hasselmann, K., T. P. Barnett, E. Bouws, H. Carlson, D. E. Cartwright, K. Enke, J. A.
Ewing, H. Gienapp, D. E. Hasselmann, P. Kruseman, A. Meerburg, P. Muller , D.
J. Olbers, K. Richter, W. Sell, and H. Walden, 1973: Measurements of wind-wave
growth and swell decay during the Joint North Sea Wave Project *(JONSWAP)*.

Hasselmann, S., K. Hasselmann, J. H. Allender, and T. P. Barnett, 1985: Computations
and parameterizations of the nonlinear energy transfer in a gravity-wave
spectrum, Part II: parameterizations of nonlinear energy transfer for application in
wave models. *J. Phys. Oceanogr*., **15**, 1378–1391.

Herbers, T. H. C., S. Elgar, and R. T. Guza, 1999: Directional spreading of waves in the
nearshore. *J. Geophys. Res*., **104**(C4), 7683–7693.

Herbers, T. H. C., T. T. Janssen, P. Jessen, D. B. Colbert, and J. H. MacMahan, 2012:
Observing Ocean Surface Waves with GPS-Tracked Buoys. *J. Atm. Ocean.*
Tech., **29**(7), 994–959.

Holthuijsen, L. H., and H. L. Tolman, 1991: Effects of the Gulf Stream on ocean waves.
J. Geophys. Res. **96**(C7) 12,755–12,771.

Irvine, D. E., and D. G. Tilley, 1988: Ocean wave directional spectra and wave-current
interaction in the Agulhas from the shuttle imaging radar-B synthetic aperture
radar. *J. Geophys. Res.,* **93**(C12), 15,389–15,401.

Janssen, T. T., and T. H. C. Herbers, 2009: Nonlinear wave statistics in a focal zone. *J.
Phys. Oceanogr*., **39**, 1948–1964.

Jonsson, I. G., 1990: Wave-current interaction. *The sea: Ocean Eng. Science. Vol. 9b.* John Wiley, Hoboken*, N.J.,* 65–120.

Khalid, M. 2012: Characterization of the vertical structure of tidal currents in the Golden Gate (San Francisco) inlet. M.S. Thesis, Graduate School of Engineering and Applied Sciences, Naval Postgraduate School, 65. http://hdl.handle.net/10945/27853

Lai, R. L., S. R. Long, and N. E. Huang, 1989: Laboratory studies of wave-current interaction: Kinematics of the strong interaction. *J. Geophys. Res.,* **94**(C11), 16201–16214.

Lai, D. Y., and D. P. Delisi, 2010: Spatial distribution of surface wave field in coastal regions using spaceborne synthetic aperture radar images. *Int. J. Remote Sensing*, **31:17-18**, 4915–4931.

Long, R. B., 1980: The statistical evaluation of directional spectrum estimates derived from pitch/roll buoy data. *J. Phys. Oceanogr.*, **10**, 944–952.

Longuet-Higgins, M. S., D. E. Cartwright, N. D. and Smith, 1963: Observations of the directional spectrum of sea waves using the motions of a floating buoy. *Ocean Wave Spectra*, *Prentice-Hall*, 111–136.

MacMahan, J., J. Brown, and E. Thornton, 2009: Low-cost Global Positioning System for measuring surf-zone currents. *J. Phys. Oceanogr.*, **25**(3), 744–754.

McIntyre, S. A., 2013: Wave and Current Observations in a Tidal Inlet Using GPS Drifter Buoys. Master's thesis, Graduate School of Engineering and Applied Sciences, Naval Postgraduate School. http://hdl.handle.net/10945/32869

Mei, C. C., 1983. *The applied dynamics of ocean surface waves*. John Wiley & Sons, 739 pp.

Melo, E., and R. T. Guza, 1991: Wave-propagation in jettied entrance channels. 2. Observations. J. *Waterway, Port, Coastal Ocean Eng.-ASCE*. **117**(5), 493–510.

NOAA – National Oceanic and Atmospheric Administration, 2009. Tides & Currents. Center for Operational Oceanographic Products and Services, http://tidesandcurrents.noaa.gov/.

Oregon State Marine Board, cited 2013: Crossing the Columbia River Bar. [Available online at http://www.oregon.gov/OSMB/library/docs/columbiamouth.pdf.]

Pearman, D. W., T. H. C. Herbers, T. T. Janssen, H. D. van Ettinger, S. F. McIntyre, P. F. Jessen, 2014: Drifter observations of the effects of shoals and tidal-currents on wave evolution in San Francisco bight, *Cont. Shelf Res.,* submitted.

Phillips, O. M., 1984: On the response of short wave components at fixed wave number to ocean current variations. *J. Phys. Oceanogr.*, **14** 1425–1433.

Phillips, O.M., 1985. Spectral and statistical properties of the Equilibrium range in wind generated gravity waves. *J. Fluid Mech*. **156**, 505–531.

Portell, J. R., 2013: Calibration and validation of inertial measurement unit for wave resolving drifters. Graduate School of Engineering and Applied Sciences, Naval Postgraduate School. http://hdl.handle.net/10945/38994.

Ris. R. C., L. H. Holthuijsen, and N. Booij, 1999: A third-generation wave model for coastal regions: Verification. *J. Geophys. Res.* **104**(C4) 7667–7681.

Rusu, L., M. Bernardino, and C. Guedes Soares, 2011: Modeling the influence of currents on wave propagation at the entrance of the Tagus Estuary. *Ocean Eng.*, **38**(10), 1174–1183.

San Francisco Port Authority, 2008: Port of San Francisco Economic Impact Study. [Available online at http://sfport.com/ftp/uploadedfiles/about_us/divisions/finance_admin/EconomicImpactReportSept2008.pdf.]

Smith, R., 1976: Giant waves. *J. Fluid Mech.* **77**(3) 417–431.

Smit, P. B., and T. T. Janssen, 2013: The evolution of wave statistics through a variable medium. *J. Phys. Oceanogr.* **43**, 1741–1758

Steele, K.E., 1997: Ocean current kinematic effects on pitch-roll buoy observations of mean wave direction and nondirectional spectra. *J. Atm. Ocean. Tech.* **14**(2), 278–291.

Thomson, J., 2012: Wave breaking dissipation observed with the "SWIFT" drifters. *J. Atm. Ocean. Tech.* **29**(12) 1866–1882.

Toba, Y., 1973: Local balance in the air-sea boundary process. III. On the spectrum of wind waves. *J. Oceanogr. Soc. Japan*, **29**, 209–220.

Vincent, C. L., and M. J. Briggs, 1989: Refraction—Diffraction of irregular waves over a mound. *J. Waterway, Port, Coastal, Ocean Eng.* **115**, 269–284.

Van der Westhuysen, A. J., M. Zijlema, and J. A. Battjes, 2007: Nonlinear saturation-based whitecapping dissipation in SWAN for deep and shallow water. *Coastal Eng.* **54**, 151–170.

Van der Westhuysen, A. J., 2012. Spectral modeling of wave dissipation on negative current gradients. *J. Coastal Eng.* **68**, 17–30.

Van der Westhuysen, A. J., A. R. van Dongeren, J. Groeneweg, G. Ph. Van Vledder, H. Peters, C. Gautier, and J. C. C van Nieuwkoop, 2012: Improvements in spectral wave modeling in tidal inlets. *J. Geophys. Res.,* **117**(C00J28), 1–23.

Wolf, J., and D. Prandle, 1999: Some observations of wave-current interaction. *J. Coastal Eng.* **37**, 471–485.

Zhang, Y. L., and A. M. Baptista, 2008: A semi-implicit Eulerian-Lagrangian finite-element model for cross-scale ocean circulation, with hybrid vertical coordinates. *Ocean Modeling,* **21**(3), 71–96.

THIS PAGE INTENTIONALLY LEFT BLANK

INITIAL DISTRIBUTION LIST

1.   Defense Technical Information Center
        Ft. Belvoir, Virginia

2.   Dudley Knox Library
        Naval Postgraduate School
        Monterey, California